

Alma Mater Studiorum - Università di Bologna

Dipartimento di Fisica e Astronomia “Augusto Righi”
Corso di Laurea Magistrale in Astrofisica e Cosmologia

**Feasibility Study of Detection and
Characterization Young Planets with
High-Resolution Spectra**

Tesi di laurea Magistrale

Presentata da:
Jiacheng Peng

Relatore:
Prof. Leonardo Testi
Dr. Lorenzo Pino

Anno Accademico 2022-2023

Abstract

Protoplanetary disks are the first stage of planet formation and evolution, which can embed young planets and embryos. Studying both the protoplanetary disks and the forming planets inside can therefore provide strong constraints into initial conditions for planet formation such as gas density and dust distribution, as well as probing the origin of planetary atmospheres.

As a crucial aspect to understand the formation scenarios and early evolution processes, it is important to observe the atmospheric emission from young planets with state-of-art high-resolution spectrometers in order to measure several physical quantities such as temperature profiles, spin rate, chemical abundance, which help to constrain the initial conditions of planet formation and early evolution.

It is always challenging to acquire spectrum from exoplanets. In particular, they are strongly contaminated by the emission from host star and strong turbulence of the earth's atmosphere, which makes it difficult to precisely observe the spectral features from exoplanets' atmosphere. High-dispersion Spectroscopy (HDS) with Adaptive Optics is a potential technique to overcome this difficulty but rarely applied. It is essential to make pre-research with simulation to understand the capability of HDS instruments on the emission of very young planets. Therefore, the objective of this project is to assess the feasibility of using the next-generation high-dispersion spectrometer CRIFES+ on VLT to study atmosphere of young planets undergoing formation processes, and help to optimize the strategies for future observations. Overall, Our results support that the spectrum of the planet HD 169142b should be detectable with the observing techniques studied in this thesis work.

Contents

1	Introduction	1
1.1	Formation and Evolution of Planets	1
1.1.1	Protoplanetary disks: formation, classification and lifetime	1
1.1.2	Giant planet formation in disks	3
1.1.3	Giant planet evolution	4
1.2	Detection and Characterization of Planets	7
1.2.1	Population of exoplanets	7
1.2.2	Atmosphere of giant planets	9
1.2.3	Detection of young planets	9
1.2.4	The planetary system HD 169142	10
1.3	Direct Imaging Techniques	11
1.3.1	High contrast imaging (HCI)	12
1.3.2	HCI combining with High dispersion spectroscopy (HDS)	14
2	Methods	17
2.1	Theoretical Spectra	17
2.2	CRIRES+ on VLT	18
2.3	Planet-to-star flux contrast	19
2.4	Pipeline to Produce Synthetic Observations	21
2.4.1	ETC computation	21
2.4.2	Principles of the reconstruction of raw images	22
2.5	Photometric system and color indexes	24
3	Results and Analysis	26
3.1	Color Diagram	26
3.2	Reconstruction of Raw Images	27
3.3	Flux contrast	27
4	Conclusion and Perspectives	33
4.1	Applying Novel Bayesian Framework	33
4.2	Future Instruments	34
4.3	Conclusion	35

Chapter 1

Introduction

Starting from the first exoplanet detected by radial velocity (RV) in 1995 by Mayor et al. 1995, our capability to detect and characterize exoplanets has experienced a transformative surge in the last three decades, leading to the identification, and characterization of thousands of sub-stellar objects and planets through a multitude of observational techniques. The diversity of exoplanet populations underlying in the large sample indicates various and complicated formation and evolution scenarios, which thus makes the formation and evolution of planets stand as an important but also challenging subject at the forefront of modern astrophysics and planetary science. Furthermore, apart from the population analysis from evolved planets, the precise spectroscopic observation of circumstellar disks (Ansdell et al. 2018), and direct-imaging of several young, self-luminous planets, opens a new observation opportunity to precisely constrain the initial conditions of planet formation and early evolution, by capturing the birth moment of planets embedded in protoplanetary disks with advanced instruments.

In this chapter, we will first introduce the fundamental theory of protoplanetary disks, planet formation and evolution, in both physics and observation. Next, we will briefly describe the detection and characterization techniques for exoplanets. In particular, in Section 1.3, we will discuss the direct-imaging techniques which is involved in this study, including High Contrast Imaging (HCI) and High Dispersion Spectroscopy (HDS).

1.1 Formation and Evolution of Planets

1.1.1 Protoplanetary disks: formation, classification and lifetime

Protoplanetary disks are disk-like structures containing gas and dust observed surrounding young stellar objects (YSO) with a few million years of the age, which are birthplaces of planets generally. From a dynamical view, the construction of protoplanetary disks is a consequence of the rotational infalling clouds towards the protostar. Taking into account a rotational energy ratio (β) as 0.02 of total energy from gravitational collapse (Goodman et al. 1993), for a $1M_{\odot}$ star with a disk radius

$r=0.05$ pc, the angular momentum J for a spherical core in rigid-body rotation is:

$$\beta \equiv \frac{E_{\text{rot}}}{|E_{\text{grav}}|} \sim 0.02 \quad (1.1)$$

$$J_{\text{core}} \simeq 10^{54} \text{ g cm}^2 \text{ s}^{-1} \quad (1.2)$$

which is significantly 3 to 4 orders of magnitude more than it can be accommodated in the total solar system, known as *the angular momentum problem* of star formation. It is thus inevitable to form a quasi-equilibrium disk so angular momentum can be redistributed with a radius r_{circ} :

$$l_{\text{core}} = J_{\text{core}} / M_{\odot} = \sqrt{GM_{\odot}r_{\text{circ}}} \quad (1.3)$$

and then transferred out of the disk via several processes including viscous accretion (Armitage 2013, Armitage and Kley 2019).

In terms of observation, the essential observation property of disks is the excess in IR continuum according to dust reprocessing of stellar radiation, which is a key observable to classify young stellar objects (YSO) associated with envelopes and disks as well as estimating the age of disks. Using the SED between mid-IR wavelengths and near-IR wavelengths, we can define the slope as:

$$\alpha_{\text{IR}} \equiv \frac{d \log \nu F_{\nu}}{d \log \nu} \equiv \frac{d \log \lambda F_{\lambda}}{d \log \lambda} \quad (1.4)$$

Based on different slope values, Armitage and Kley 2019 classified the YSO from Class 0 to Class III corresponding to different evolution stages as follows:

- Class 0: (α_{IR} undefined because of sources heavily obscured from optical or near-IR emission.
- Class I: $\alpha_{\text{IR}} > 0.3$.
- Flat spectrum sources: $-0.3 < \alpha_{\text{IR}} < 0.3$.
- Class II: $-1.6 < \alpha_{\text{IR}} < -0.3$.
- Class III: $\alpha_{\text{IR}} < -1.6$. with very weak IR-excess emission and SEDs that close to isolated pre-main-sequence stellar photospheres.

The distribution of known YSOs is shown in Fig. 1.1. Generally, the protoplanetary disks can be resolved when the free-falling stage of envelope is almost finished, i.e. when the envelope is largely vanished during infalling to feed the rotational protoplanetary disk, corresponding to Class II or Class III in observation.

Protoplanetary disks evolve through a variety of processes, including viscous transport, photoevaporation by the central star, grain growth and dust settling, and dynamical interaction with (sub)stellar and planetary-mass companion (Williams et al. 2011). Therefore, it is difficult to precisely and analytically compute the disk lifetime. Infrared surveys can help us to roughly estimate it from observation point of view. Early studies focusing on the fraction of stars with IR excess as a function of stellar ages implies that the disk fraction gradually decrease from 80% to 10% over 10 Myr. Notably, the disk lifetime establishes a strong constraint for gaseous planet formation processes that is expected to accomplish before the total dissipation of gaseous disk.

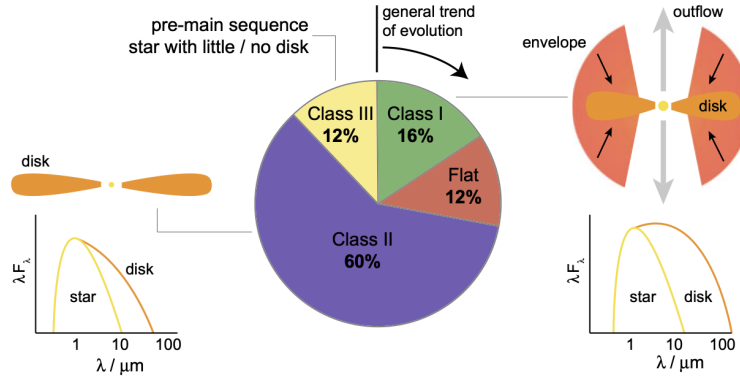


Figure 1.1: The distribution and sketches of YSOs. There is not clear definition of protoplanetary disks, but they are usually isolated from the protostars of Class II YSO and hence can be spatially resolved and observed, according to Armitage and Kley 2019.

1.1.2 Giant planet formation in disks

The protoplanetary disks are regarded as the birthplace of planets. In the past few decades with the development of multi-wavelength instruments such as SPHERE on VLT and ALMA, several protoplanets or candidates embedded in disks are found by imaging (Mesa et al. 2019, Hammond et al. 2023, Kalas et al. 2008), and indirect evidence including gaps in disks, wrapped and distorted disks (Stasevic et al. 2023, Dawson, Murray-Clay, et al. 2011, Pinte et al. 2019), and the twist spiral waves (Boccaletti et al. 2020) are observed and linked with planet formation.

For gas giant planet formation, a popular and widely applied paradigm is core accretion, so-called Bottom-up scenario first described by Perri et al. 1974 and Mizuno 1980. An initial seed solid core forms in accretion of planetesimals or pebbles to form an embryo. Until the embryo goes over a certain critical mass the gravity of the core becomes high enough that a hydrodynamical instability is triggered that results in a rapid, runaway gas accretion onto the core, and thus eventually to the formation of a gaseous giant planet (Armitage 2013, Armitage and Kley 2019, Perryman 2018). The core accretion mainly consists of four phases as shown in the sketch Fig. 1.2. The evolution mass and luminosity of both the core and the envelope considering core-accretion is developed in several models. Fig. 1.3 illustrates a popular one from Pollack et al. 1996.

Phase 1 is the phase of core formation, which the core rapidly accretes planetesimals or pebbles until reaching its maximum mass, i.e. isolation mass. Next, in *Phase 2* the decrease of solid accretion results in a decrease of luminosity, which leads the envelope to contract since lack of radiation pressure, hence more gas can be accreted. This is envelope accretion phase, whereas the core mass can slightly increase because the total mass of planet keeps increasing, enlarging the Hill Sphere to allow more solid to be accreted. *Phase 3* begins when the core eventually crosses its critical mass and meanwhile envelope mass being comparable with core mass, hydrodynamical instability generates and results in the runaway of gas accretion. At a certain point the gas accretion required by the cooling of protoplanets' interior

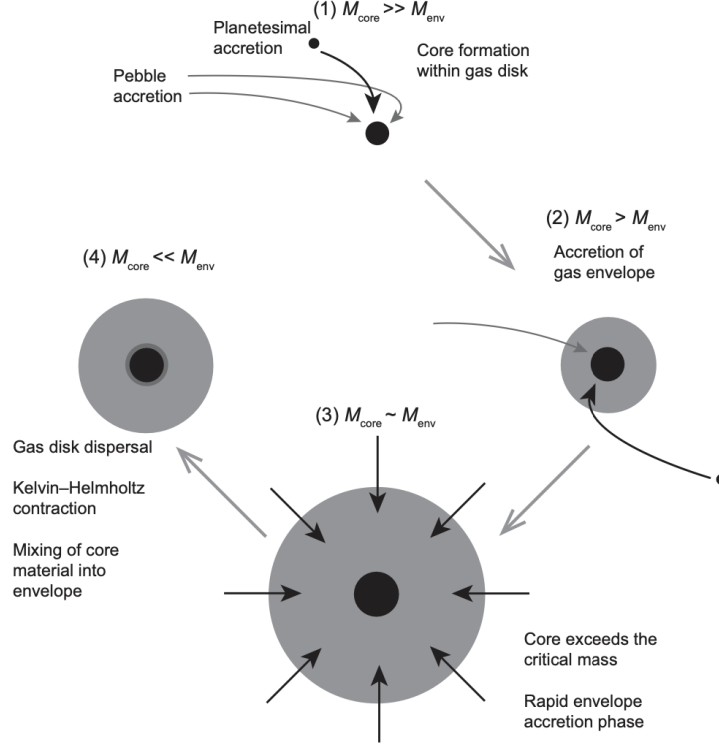


Figure 1.2: Four phases for the formation of gaseous giant planet in core accretion model, from Armitage 2013.

exceeds the amount of gas can be supplied by the protoplanetary disk, i.e. the gas supply is exhausted (Armitage 2013), then the planet detaches from the disk but can still keep viscous accretion. The termination of gas accretion is related to several factors. First, for $M_P > 1M_J$, the local gap can be open during orbiting (Paardekooper et al. 2004) when the Hill radius is beyond the height of the disk: $R_H \geq H$ (Perryman 2018), which furthermore dampen the viscous accretion (Tanigawa et al. 2008) and therefore terminate the formation. In addition, the dissipation of gas disk also plays a role as the reservoir of gaseous component sets up the natural upper limit of mass. The last phase is known as the termination phase, i.e. *Phase 4*.

Besides the gap opening which is able to be imaged in protoplanetary disks, the contraction of envelope leads to a drastic increase of luminosity during *Phase 3* illustrated in Fig. 1.3b, promoting the protoplanet into a self-luminous regime that can be detected and observed with telescopes conducted state-of-art techniques. It will be discussed later.

1.1.3 Giant planet evolution

As shown in Fig. 1.3, the classic core accretion model considers planet formation at a few A.U. or beyond and circular orbits, whereas many exoplanets detected illustrated in Fig. 1.6 and 1.7 are inconsistent with these assumptions, including

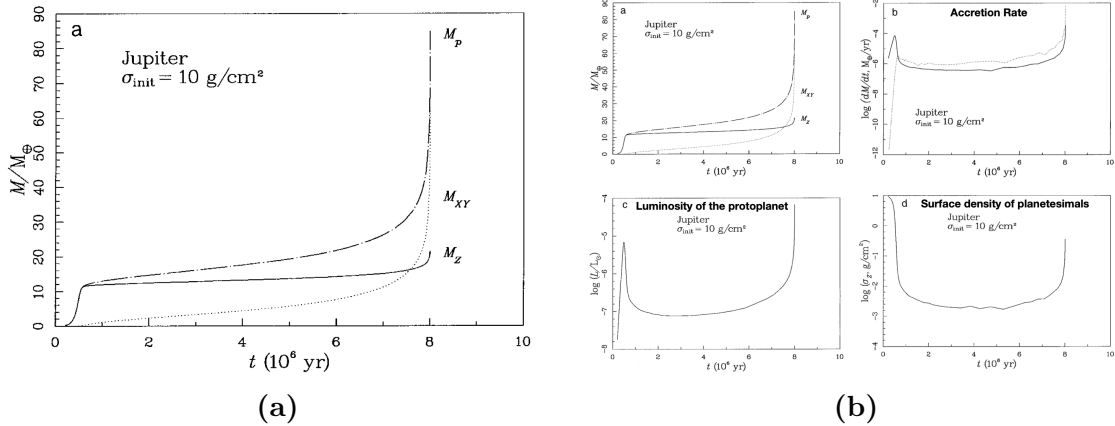


Figure 1.3: (a): The mass evolution from Phase 1 to Phase 3 in core accretion for Jupiter ($M = 1M_J, d = 5.2AU$) for Pollack96 model. M_P is the total mass of the planet. M_Z presents the core mass considering heavy elements and M_{XY} is the mass of envelope that consist of Hydrogen (X) and Helium (Y). (b): The luminosity, surface density of planetesimals and the accretion rate evolution in Pollack96.

giant planets which are extremely close to the host star such as hot Jupiters, and planets with large eccentricity or located in chaotic orbits. The population related to this work, namely the self-luminous planets discovered by direct-imaging at very large separation from host stars comparing with the Solar System (Fig. 1.10). Furthermore, young planets observed by direct-imaging are found with grossly higher effective temperature (from warm to hot giants, $T_{eff} > 1000K$ (Dawson and Johnson 2018)) than many giant planets as well as those in the Solar System. All of these evidences support a evolutionary history of planets both in kinematics related to migration, and thermodynamics related to internal cooling, which eventually distinguish evolved planets from young planets.

From a dynamical point of view, the primary mechanism of evolution is migration. Concentrating on the early evolution for giant planets when embedded in the gaseous disk, planets exchange energy and/or angular momentum with the gas components under planet-disk interaction. The presence of planet perturbs the density of the disk. The asymmetry of disk density generate a torque Λ on the planet. Taking into account the disk as a superposition of sound waves, then the strongest perturbation exits at particular resonances (Armitage 2013), most importantly at the co-rotation resonance and Lindblad resonance (Binney et al. 2008):

- co-rotation resonance: The co-rotation torque occurs at horseshoe regions where :

$$\Omega(r) = \Omega_p \quad (1.5)$$

Ω_p is the angular frequency of the planet. $\Omega(r)$ is the orbital frequency of is disk.

- Lindblad resonance: Inner and outer Lindblad resonances occur for:

$$m [\Omega(r) - \Omega_p] = \pm \kappa(r) \quad (1.6)$$

$\kappa(r)$ is the epicyclic frequency. For Keplerian obrits, $\kappa(r) = \Omega(r)$. So the radii

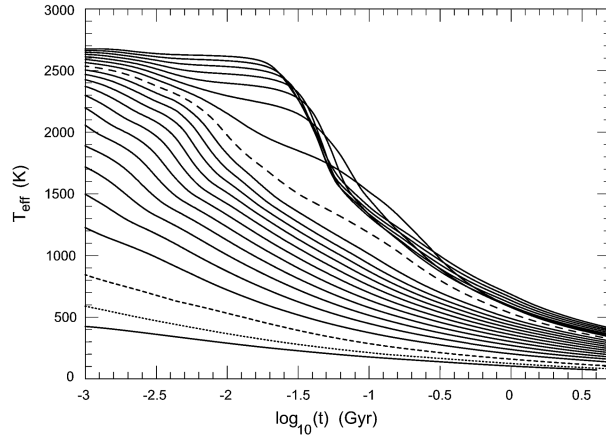


Figure 1.4: The effective temperature versus age (in Gigayears) for giant planets with masses of (from bottom curve) $0.3 M_J$, $0.5 M_J$, $1.0 M_J$ in dashed lines, respectively and from 2.0 to $20.0 M_J$ in steps of $1.0 M_J$, from Hubbard, Burrows, et al. 2002

of Lindbald torque taking place are:

$$r_L = r_p \left(1 \pm \frac{1}{m} \right)^{2/3} \quad (1.7)$$

The net effect of two torques plus additional torques due to thermal effect lead two main types of migration for planets, depending on the mass of planets. For gas giants that are capable for gas opening, it usually refers to *Type II migration*, which provides a mechanism to allow gas giants formed beyond snow lines to migrate inwards in a long timescale associated with a annular gap that can also be observed from the disk iamges from ALMA (Andrews et al. 2018).

Giant planets undergo thermal evolution as well. Planets are capable to keep hot and luminous soon after the termination of accretion. As the nuclear reactions are not ignited inside the core, they cool and radiate away their heat, accordingly the interiors and atmospheres undergo various changes, such as differentiation, solidification, and condensation which are able to change the global opacity, form dusty clouds, generate greenhouse effect or sink processes (Hubbard, Guillot, et al. 1999, Hubbard, Burrows, et al. 2002, Burrows et al. 1997) and therefore lead to non-linear and complicated thermal evolution. The rate of cooling depends on multiple factors such as the planet’s gravity, age, and composition, as well as the efficiency of energy transport and the opacity sources in its atmosphere. As plotted in Fig. 1.4, it takes 1 Gyr for a Jupiter-like planet ($M_P \sim 1M_J$) to cool down from 800K to present-day effective temperature of Jupiter as around 106K. And in reality Jupiter is still in cooling after 4.5 Gyr. Similar study from Burrows et al. 1997 illustrates evolutionary tracks of density and gravity versus effective temperature for planets and sub-stellar objects, plotted in Fig. 1.5.

However, coupled with the migration and other mechanisms in dynamics, the thermal evolution of giant planets might become more complicated. For example, varying solar insolation at different radii may change the situation of external heating for evolved planets which links to the population of hot Jupiters (**hot Jupiter**).

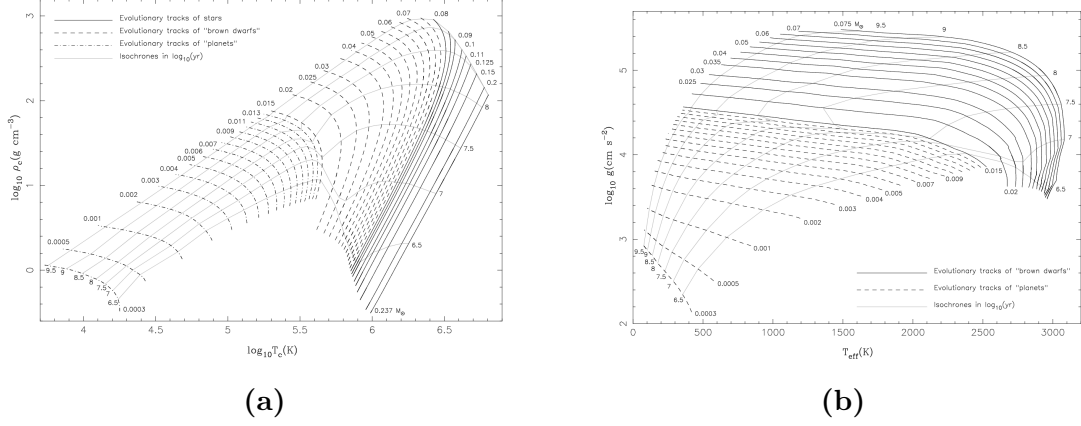


Figure 1.5: (a) Density vs. effective temperature evolution tracks from solar-mass objects to planets. (b) Similar to (a) but gravity vs. effective temperature evolution tracks, from Burrows et al. 1997.

For a more precise study in evolution, tidal heating atmospheric escape might be considered as well.

1.2 Detection and Characterization of Planets

1.2.1 Population of exoplanets

Exoplanets can be classified based on mass and radius comparing with planets from the Solar System, indicating the difference of composition. Here we introduce the categories used in Zeng et al. 2019 , as plotted in Fig. 1.6.

- Rocky worlds: ($< 2\mathbf{R}_{\oplus}$).
- Water worlds: ($2 - 4\mathbf{R}_{\oplus}$).
- Transitional planets: ($4 - 10\mathbf{R}_{\oplus}$).
- Giant planets: ($> 10\mathbf{R}_{\oplus}$).

\mathbf{R}_{\oplus} is Earth radius. Gas giants are comparable with Jupiters in mass and radius. The mass of giant planet can rise up to $\sim 14M_J$ which Deuterium ignites.

In this work we focus on utilizing direct-imaging to observe the population of young planets, which requires a high effective temperature leading a high flux contrast ratio with respect of stellar emission, a relatively large angular separation (comparing with planets detected by Transit or Radial Velocity) to be spatially separated from diffraction limit. Thereby the favorable population under this detection technique are giant planets, consistent with the Fig. 1.6 and the orbital distance-Mass diagram of Fig. 1.7. Overall, direct-imaging is generally more sensitive to young giant planets instead of other three populations with young age. It is reasonable to set up simulation following giant-planet characteristics later in Section 2.1. We will go back for direct-imaging techniques in Section 1.3.

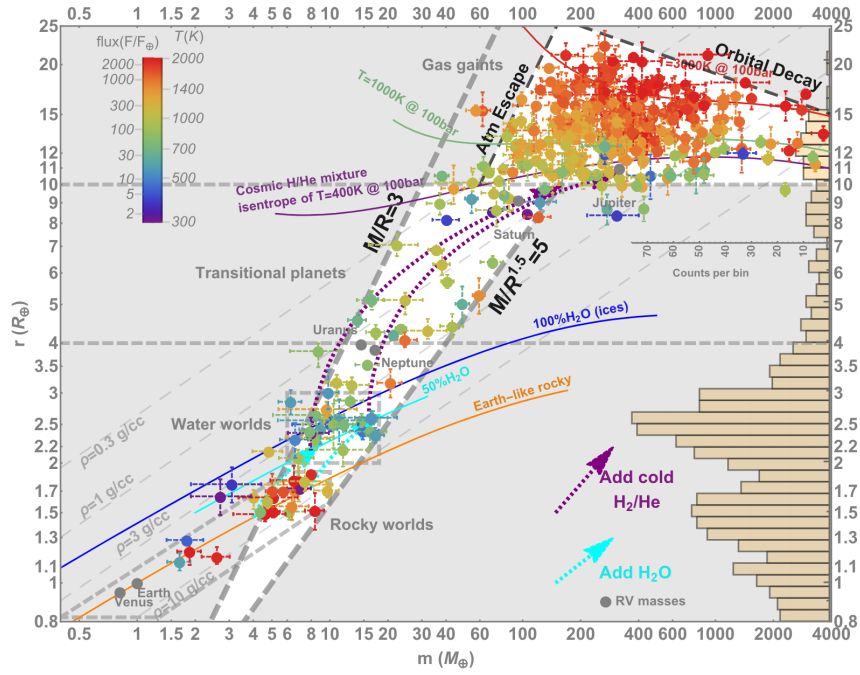


Figure 1.6: The Mass-Radius diagram from Zeng et al. 2019 which associated with composition curves and denoted with effective temperatures.

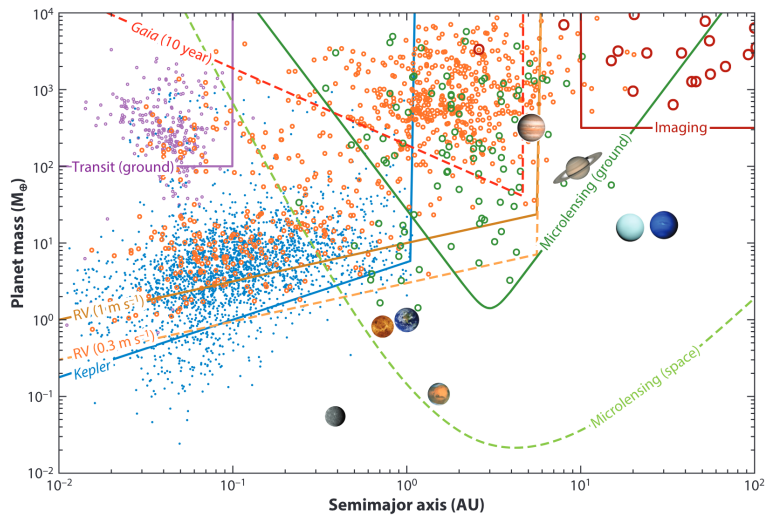


Figure 1.7: The Mass-Distance diagram of detected exoplanets from Zhu et al. 2021

1.2.2 Atmosphere of giant planets

As described in Section 1.1.2, giant planets accumulate a large amount of gas during gas runaway phase to form thick atmospheres that consist of various components including H₂O, CH₄, CO, CO₂ and hot dust grains like Al₂O₃ (France Allard et al. 2001, F. Allard et al. 2011). Different components are dominant at different height to form layers. Thus, the intensity of atmosphere can be computed by radiative transfer:

$$\mu \frac{dI(z, v, \mu, t)}{dz} = -\kappa(z, v, t)I(z, v, \mu, t) + \varepsilon(z, v, \mu, t) \quad (1.8)$$

I is the intensity [$\text{Jm}^{-2} \text{s}^{-1} \text{Hz}^{-1}$]; κ is the absorption coefficient [m^{-1}]; ε is the emission coefficient [$\text{Jm}^{-3} \text{s}^{-1} \text{Hz}^{-1}$]; $\mu = \cos \theta$ and θ is the angle away from surface normal; and $z = z(T, P)$ is vertical altitude. This formula becomes the fundamental formula for 1-D model of atmospheric emission considering the optical depth τ , $d\tau = -\kappa dz$:

$$\mu \frac{dI(\tau, \lambda, \mu, t)}{d\tau} = -\kappa(\tau, \lambda, t)I(\tau, \lambda, \mu, t) + B(\tau, \lambda, t). \quad (1.9)$$

After the formation of planet, we can assume local thermodynamical equilibrium and thus apply black body function B (Seager et al. 2010). From Kirchoff's law we know $B = \varepsilon/\kappa$.

The absorption coefficient and emission coefficient are the essentials to determine the theoretical spectra, which are controlled by the opacity, chemistry and clouds in atmosphere:

$$\kappa(\lambda, T, P) = n(T, P)\sigma(\lambda, T, P) \quad (1.10)$$

where n is the number density of one gas component which is given from chemistry equilibrium for simplification, and σ is the cross-section. Notably, at a given wavelength, all existing gas components must be included for κ .

Cloud formation differentiate sub-stellar atmosphere (brown dwarfs, giant planets) from stellar atmosphere. According to the chemistry equilibrium and the condensation temperatures of different molecules, the cloud is composed from ZrO₂ finally to ices (H₂O, NH₃, NH₄SH). When the effective temperature is lower than 2200K, global mixing needs to be taken into account as a consequence of cloud convection generated by cloud layers which are already enough optically thick. This effect is considered in BT-Settl model developed by F. Allard et al. 2012 utilized in this work.

1.2.3 Detection of young planets

There is no strict definition of *young planets*. The age of the host star establishes an upper limit of planets' age in the system, therefore in general planets orbiting Pre-MS stars (Charbonnel et al. 2008) can be regarded as young planets. To be more precise, it can refer to those embedded in the circumstellar disks including mostly protoplanetary disks, and also transition disks and debris disks. Those planets probably still undergoes formation processes or planet-disk interactions, and so-called "protoplanets" in some contexts.

Up to 2020, there are 49 planets detected by direct imaging based on the catalog

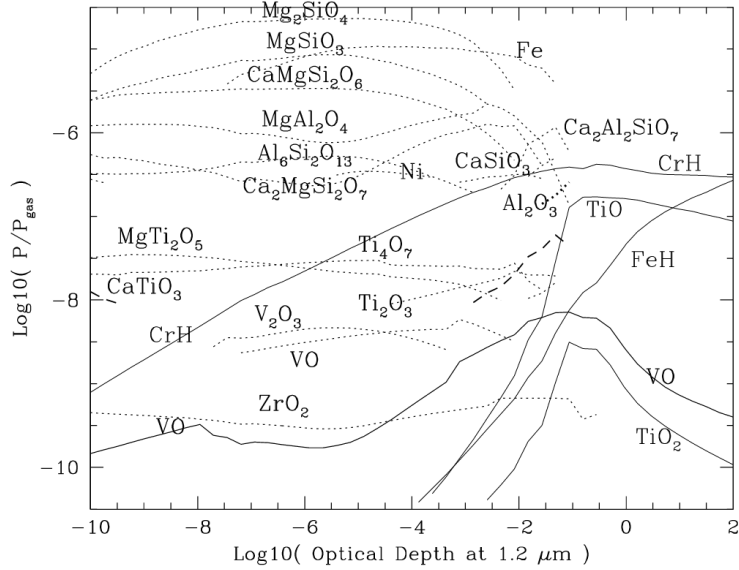


Figure 1.8: The model atmosphere of relative abundances for gas components from the AMES (France Allard et al. 2001), with $T_{eff} = 1800K$.

from NASA Exoplanet Archive¹ as plotted in Fig. 1.10, and circumstellar disks are detected in 24 of them which can be recognized as young planets, illustrated in Table. 1.4. The age ranges from five to hundreds of Myrs. We choose the planetary system HD 169142 since the planet is embedded in the protoplanetary disk. Thus it enables us to study the mission furthermore close to the birth moment of planetary atmosphere².

1.2.4 The planetary system HD 169142

The target planetary system in this feasibility study consists of a young, pre-MS star hosting a newly detected planet (Quanz et al. 2013, Hammond et al. 2023) embedded in the disk. The host star is a Herbig Ae star surrounded by a face-on ($i = 13^\circ$) protoplanetary disk. The main properties measured from Gaia DR3 are shown in Table 1.1. Notably, according to the analysis based on several archived observations in Saffe et al. 2021, HD 169142 keeps λ Bootis pattern which describe a peculiar kind of stars with significantly low Fe abundance of 1 -2 dex lower than the solar one, but near-solar abundance for other metal elements such as C, N, O, S, which can explain the low value in Gaia DR3 measurement of Fe abundance, even though the inconsistency is still larger than expected.

The planet itself is a Jovian-mass protoplanet located at a radius of 37 AU from the star, and is enshrouded in a significant amount of dust. An outer spiral arm is also observed indicating ongoing accretion processes, which makes the planet as a good example to study the atmospheric emission of young planets, thereby to help understand and constrain the formation conditions of planets. The information of

¹Online Catalog for direct-imaging planets

²The target system HD 169142 is not listed in Table 1.4 since the planet is just confirmed in 2023

Table 1.1: Physical Quantities of HD 169142

Physical Quantity	Value
Mass	$1.85 M_{\odot}$
Spectral type	F1V
Age	6.0 ± 1.0 Myr
Distance	114.8 pc
Absolute Magnitude	$2.7262 \sim 2.7496$ mag
Effective temperature	$7204.7563 \sim 7216.1562$ K
Metallicity	$[\text{Fe}/\text{H}] = -1.884$
Gravity	$\log(g) = 4.1115 \sim 4.1183$ cm s ⁻²
Classification	Herbig Ae/Be Star

Table 1.2: Physical Quantities of HD 169142 b

Physical Quantity	Value
Projected angular separation	0.319 arcsec
Projected spatial separation	~ 37 A.U.
Y band planet-to-star contrast	$1.49 \times 10^{-5} \pm 5.95 \times 10^{-6}$
J band planet-to-star contrast	$1.73 \times 10^{-5} \pm 6.16 \times 10^{-6}$
H2 band planet-to-star contrast	$1.93 \times 10^{-5} \pm 1.17 \times 10^{-5}$

HD 169142b derived from SPHERE IFS by Hammond et al. 2023 is presented in Table 1.2. The confirmation image is plotted in Fig. 1.9.

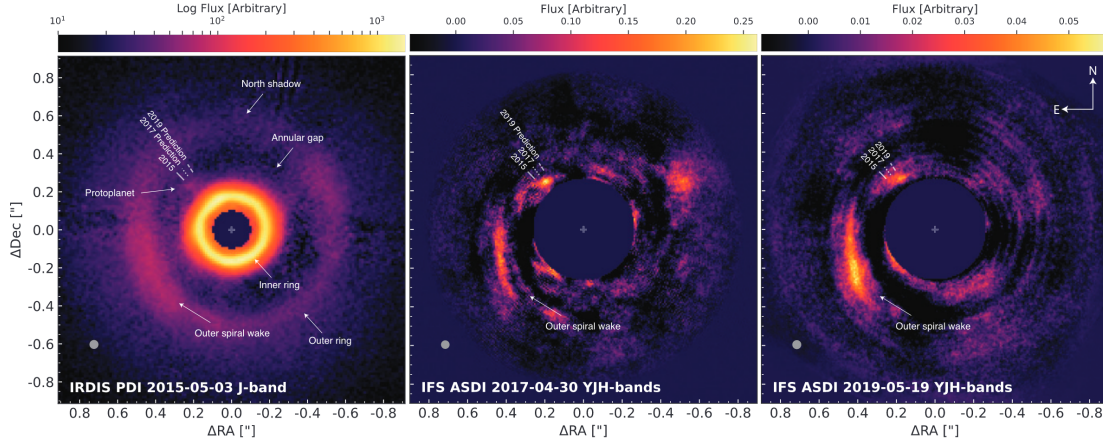


Figure 1.9: The coronagraphy image for HD 169142b observed with SPHERE IFS at near-IR band, from Hammond et al. 2023.

1.3 Direct Imaging Techniques

Direct-imaging refers planets as point sources reflecting or irradiating flux, and aim to spatially resolve the targets from the host star to obtain images and spectra of

them. There are two aspects to constrain the feasibility of direct imaging, angular separation (a) and flux contrast (Perryman 2018).

The projected angular separation between is defined as:

$$\theta_{\max} = \frac{a(1+e)}{d} \quad (1.11)$$

where d is the distance from the Earth. To be capable to be observed, the angular separation of planet must be larger than diffraction limit angle $\Delta\theta$ of the stellar light, known as Raleigh Criteria:

$$\Delta\theta[\text{rad}] > 1.22\lambda/D \quad (1.12)$$

where D is the diameter of the single-pupil telescope. In CGS unit:

$$\theta[\text{arcsec}] > 0.252 \frac{\lambda[\mu\text{m}]}{D[\text{m}]} \quad (1.13)$$

Furthermore, for ground-based telescopes such as VLT, the turbulence of the Earth's atmosphere degrade the quality of images and spectra, changing the detection from diffraction-limit regime to seeing-limit regime. Atmospheric seeing can be defined as:

$$\theta \propto \lambda/r_0 \quad (1.14)$$

r_0 is Fried parameter: $r_0 \propto \lambda^{6/5}$.

The flux contrast between the planet (f_p) and the star (f_*) is also crucial to limit the capability of direct-imaging. For self-luminous planets, we neglect the phase difference and regard the planet and the host star as two sources with different effective temperatures, the theoretical flux contrast R is:

$$R = \frac{f_p(\lambda)}{f_*(\lambda)} = \frac{B_p(\lambda)}{B_*(\lambda)} \left(\frac{R_p}{R_*} \right)^2 \quad (1.15)$$

where B is the Plank Function. A practical form of R used in this simulation pipeline will be discussed in Chapter 2.

The techniques engaged into direct-imaging are all aimed to reduce the blurring of seeing, and/or dampen the photon noise from the host star to promote the flux contrast, and eventually resolve the planet from the host star, and enhance the SNR of images and spectroscopy for furthermore analysis. The most popular two are High-contrast Imaging (HCI) and High-dispersion Spectroscopy (HDS).

1.3.1 High contrast imaging (HCI)

Adaptive Optics (AO)

Adaptive optics aims to compensate the turbulence of the Earth's atmosphere to promote the angular resolution from seeing-limit to diffraction-limit. By continuously measuring the wavefront of a reference star near to the target and/or laser guide stars, with a frequency of 1kHz, AO system is able to analyze and produce an opposite wavefront correction on the deformable mirror. The sketch workflow of a

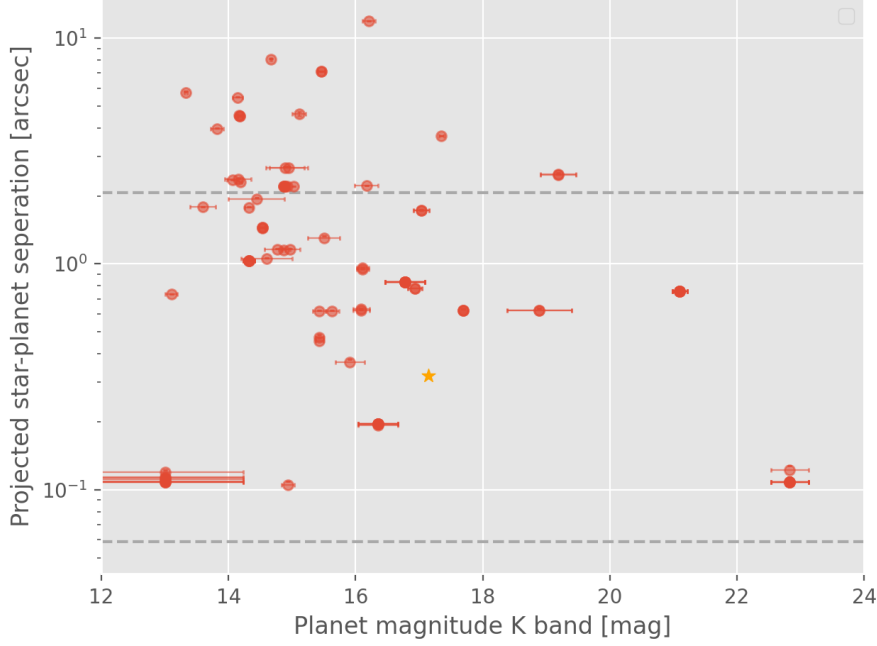


Figure 1.10: Direct imaging planets included in the NASA Exoplanet Archive (until 2020). The orange star denotes the location of HD 169142b on this Ks brightness-angular separation plot. The lower and upper gray dashed lines marks the angular size of one pixel of the detector, and the largest extraction aperture size for CRIFRES+, respectively.

typical AO system is shown at Fig. 1.11. Davies et al. 2012 reviews the role of AO in modern astrophysics with technical details. Strehl ratio is often used to access the performance of a AO system:

$$\text{Strehl ratio} = \frac{I_{max,measured}}{I_{max,diffraction-limit}} \quad (1.16)$$

MACAO on VLT can reach Strehl ratio around 50%, while SPHERE conducted extreme AO can reach 90% (Beuzit et al. 2019).

Coronagraphy

Coronagraphy is not installed on CRIFRES+. But it is worthwhile to introduce the technique since the detection of many young planets by direct-imaging is actually done by coronagraphy, and it is possible to consider it as part of our synthetic observation pipeline in the future. Coronagraphy was firstly implemented on telescope for observation of the solar corona (Lyot 1939). The idea for detection of exoplanets is therefore to intercept more light from the host star by coronagraphic masks and allow more emission from the companion to incident onto the focal plane. The workflow of a classic coronagraph is illustrated in Fig. 1.12. Coronagraphs require precise data reduction to remove spekle noise which are from the aberration of the optical system and can mimic the signal of faint planets. Several methods are applied to achieve this goal such as Angular Differential Imaging (ADI), Spectral Differential Imaging (SDI), etc.

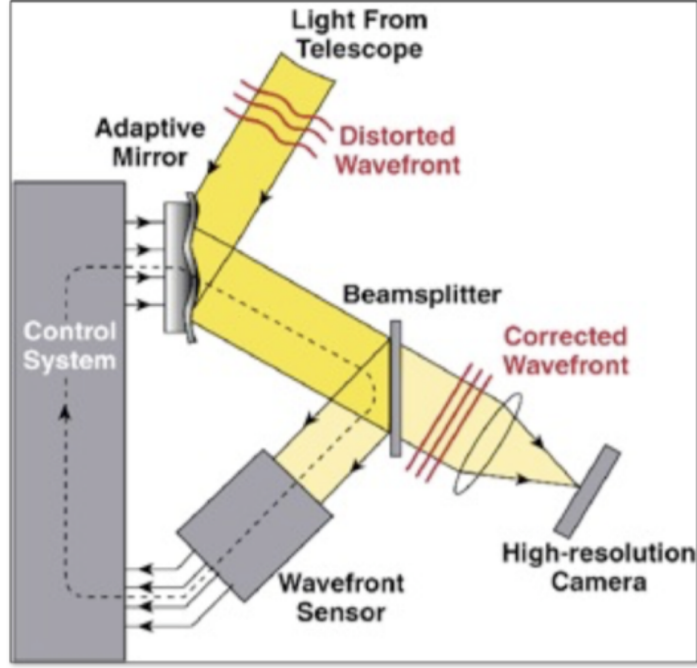


Figure 1.11: The sketch of a typical AO system. Courtesy: CFAO/Lawrence Livermore National Laboratory

As a result, HCI in combination with both AO and coronagraphy plays an important role to directly image the planets in the last decade. Various instruments such as SPHERE, GPI and NACO lead to a diverse detection of giant, luminous sub-stellar objects. However, current HCI instruments can only produce low-resolution spectra which is difficult to precisely characterize the atmosphere on planets. For example, The integral field spectrograph (IFS) on SPHERE keeps resolution $R \sim 30$ at $0.95 - 1.65 \mu m$ and $R \sim 50$ at $0.95 - 1.35 \mu m$ (Claudi et al. 2008).

1.3.2 HCI combining with High dispersion spectroscopy (HDS)

According to Birkby 2018 and Snellen et al. 2015, HCI ensures the capability of resolving wide-orbit self-luminous planets from the host star to acquire a known projected separation. High-resolution spectroscopy further increase the signal-to-noise of the planet by combining many of its spectral lines via cross-correlation. By combining both techniques, it is possible to spatially resolve the planet and star as two separated sources on the spectroscopy slit. The fainter planet spectrum is expected to be detected in one row. Hence, by removing the stellar signal and telluric lines using the template generated from stellar-only rows, ideally the signal of planet is the only astronomical signal left on the detector plane. Next, utilizing the spectral line template to cross-correlate with the planetary signal, the SNR can be significantly boosted and lead to the detection of emission lines from the planet's atmosphere which physical properties can thus be analyzed. The SNR in HCI+HDS

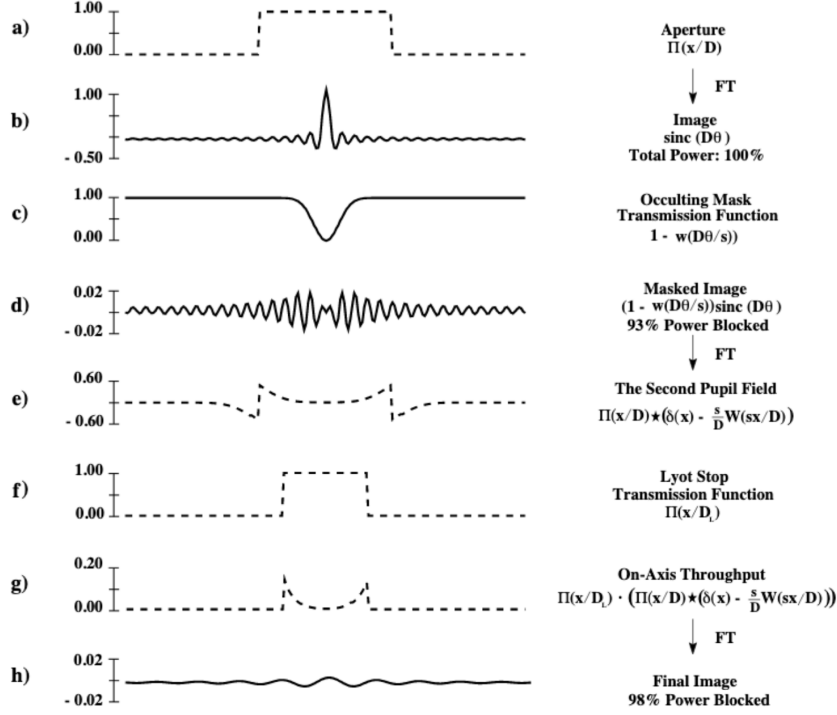


Figure 1.12: The workflow of a classic coronagraphy system from Sivaramakrishnan et al. 2001. After rejection and correction 99% of stellar light can be removed.

processing can be written as:

$$\text{SNR}_{\text{planet}} = \left(\frac{S_p}{S_\star} \right) \text{SNR}_{\text{star}} \sqrt{c_{\text{HCI}} N_{\text{lines}}} \quad (1.17)$$

where c_{HCI} is the suppression factor from HCI. N_{lines} is the number of emission lines for one molecule detected in the observed wavelength range. Snellen et al. 2015 modelled the planet-to-flux contrast ratio limit in combination of HCI and HDS shown in Fig. ??, suggesting that HDS+HCI can reach to the contrast down to 10^{-7} .

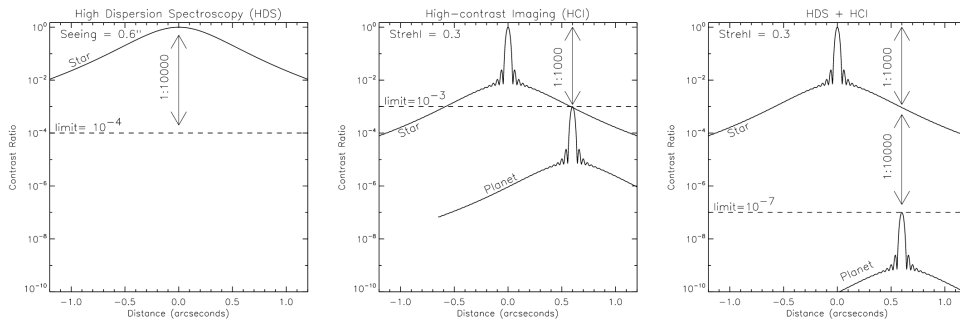


Figure 1.13: A toy model shows the contrast ratio with the angular distance between two objects applying different technologies, from Snellen et al. 2015.

Table 1.3: Direct-imaged planets detected with circumstellar disks

name	ra	dec	J mag	ΔJ mag	K mag	ΔK mag	a (arcsec)	a (AU)	T_{eff}
bet Pic b	86.8212	-51.066513					0.411	7.9	1400.0
2MASS J12073346-3932539 b	181.88945	-39.548332	18.5	5.5	16.93	4.98	0.778	55.0	1250.0
GQ Lup b	237.30043	-35.65142					0.733		
HR 8799 c	346.86966	21.13425	17.63	12.25	16.11	10.87	0.95	37.4	1090.0
HR 8799 b	346.86966	21.13425	19.28	13.9	17.03	11.79	1.73	68.2	870.0
Fomalhaut b	344.4127	-29.622236					12.7	97.6	
FU Tau b	65.89891	25.049898			13.33		5.72	800.8	2375.0
Oph 11 b	245.60506	-24.087208	15.86	0.82	14.44	0.52	1.943	242.9	2175.0
HN Peg b	326.13055	14.771939	15.86		15.12		43.2	795.0	1130.0
USco CTIO 108 b	241.47533	-18.312332	16.53	3.11	15.11	2.6	4.6	670.0	2350.0
HR 8799 d	346.86966	21.13425	18.24	12.86	16.09	10.85	0.63	24.8	1090.0
1RXS J160929.1-210524 b	242.37627	-21.083036			16.17	7.25	2.219	330.0	1800.0
2MASS J04414489+2301513 b	70.43707	23.030941			14.94	1.54	0.105		
HR 8799 e	346.86966	21.13425			15.91	10.67		14.5	
HD 95086 b	164.26259	-68.66734			17.69		0.624	56.4	1000.0
PDS 70 b	212.04233	-41.397938			16.35	7.81	0.195	22.0	1200.0
2MASS J01225093-2439505 b	20.712242	-24.66405	16.81	5.8	14.53	5.36	1.45	52.0	
HD 106906 b	184.47163	-55.975525	17.6	10.7	15.46	8.78	7.11	654.1	1800.0
HD 100546 b	173.356	-70.194786			15.43	9.6	0.457	53.0	932.0
LkCa 15 b	69.82415	22.350967					0.106	14.7	
51 Eri b	69.40055	-2.4735482	19.09	14.35			0.449	13.2	675.0
LkCa 15 c	69.82415	22.350967					0.068	18.6	
HR 2562 b	102.50423	-60.249146					0.619	20.3	1200.0
PDS 70 c	212.04233	-41.397938				8.8	0.277	27.2	

Chapter 2

Methods

This chapter will present the methodology that is followed to produce synthetic VLT/CRIRES+ observations of putative spatially resolved exoplanets. These synthetic observations are built starting from a library of theoretical models for 1-D spectra, presented in Section 2.1 that will later input into a pipeline to generate 2-D raw images in combination with stellar light and sky background assuming a specific position for planet, and also to compute the planet-to-star flux contrast ratio and relevant quantities, discussed in Section 2.3. Principles and design of the pipeline will be introduced in Section 2.4. Besides the simulation, the synthetic observation also consists of the color analysis which methodology will be presented in Section 2.5.

2.1 Theoretical Spectra

The BT-Settl model is a widely used theoretical model for studying the atmospheres of low-mass stars, brown dwarfs, and giant exoplanets. This model, developed by F. Allard et al. 2012, combines the principles of radiative-convective equilibrium, atmospheric opacities, and chemical equilibrium to predict the spectra of these objects across a broad range of effective temperature, surface gravity, and metallicity as input parameters. The BT-Settl model also input molecular line lists and continuum opacities, enabling reliable predictions of theoretical spectra of stellar and sub-stellar objects including the contribution of various molecule such as absorption bands of methane, water vapor (Barber et al. 2006), and other potential components in the atmosphere of stellar/sub-stellar objects i.e. clouds and dust. Overall, it is a robust tool for studying the feasibility of spectroscopic observations for giant planets in a diversity of configurations by adjusting the three input parameters, effective temperature T_{eff} , gravity $\log(g)$ and bulk metallicity M .

As the parameters of young planetary system HD 169142 is poorly known due to the limited capability of previous observation discussed in Section 1.2.4, the input parameters for the planet are based on the confirmed young planet PDS 70b. Wang et al. 2021 fit the spectrum of PDS 70b obtained with VLT GRAVITY with a suite of models (Table 4 of Wang et al. 2021), and reported a good SED fitting with BT-Settl added ISM extinction and a second blackbody component at longer wavelength, indicating the absorption and re-radiation of protoplanet's light by the surrounding disk, with $T_{eff} = 1392_{-82}^{+82}\text{K}$, $\log(g) = 3.83_{-0.32}^{+0.69}$, $R = 1.96_{-0.17}^{+0.20}R_{Jup}$.

Table 2.1: Input parameters for Generating SED. The step is 0.5 for $\log(g)$ and 100K for T_{eff} .

	Host star	Companion
Metallicity	0	0
$\log(g)$	4.0	3.5-5.5
T_{eff} (K)	7250	1000-2000

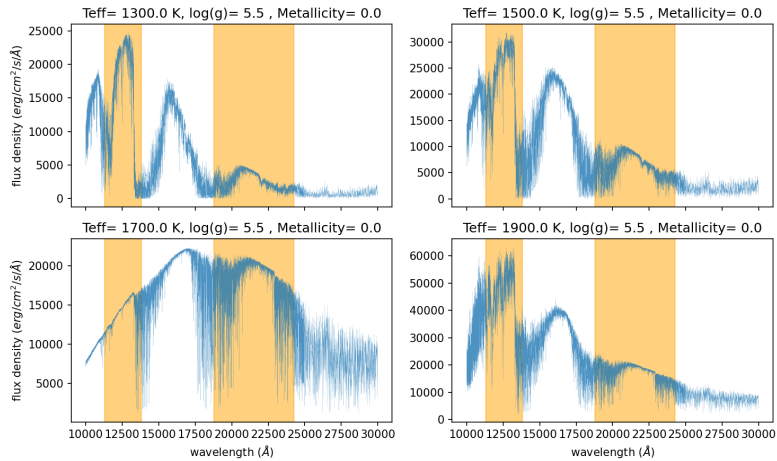


Figure 2.1: BT-Settl generated spectra from $1\mu m$ to $5\mu m$, with T_{eff} =1300K, 1500K, 1700K and 1900K and $\log(g)$ =5.5, Metallicity=0.0. The orange color covers the J band and Ks band involved in the color index computation.

Thus, for the purpose of this thesis work, the effective temperature T_{eff} is taken from 1000K to 2000K, which includes the best-fit temperature of PDS-70b found by Wang et al. 2021, and is consistent with hot giants reaching its peak flux in K band (Seager et al. 2010). Given the peculiar metallicity patterns of the host star discussed in Section 1.2.4, for simplification, we set up the bulk metallicity as solar metallicity which is consistent with the abundances of heavy elements such as C, N and O of the host star. While the iron abundance of the host star is obviously sub-solar, the contribution of Fe in the near-Infrared wavelength range targeted by CRIRES+ is negligible (France Allard et al. 2001). In addition, the gravity $\log(g)$ is set up from 3.5 to 5.5, including most values from PDS 70b modelling. Furthermore, we use MARCS template spectra (Gustafsson et al. 2008) to generate the SED of the host star. We also set the metallicity for the host star to solar, for simplification. The input parameters used for simulating the theoretical spectra of both the star and the planet is shown in Table 2.1. In total, these input parameters combine into 55 spectra for the planet with the host star. One example is shown in Fig. 2.1.

2.2 CRIRES+ on VLT

CRIRES+ (Cryogenic Infrared Echelle Spectrograph Plus) is an advanced cross-dispersed Echelle spectrograph designed for high-resolution infrared observations upgraded in 2014 from the original version CRIRES (Kaeufl et al. 2004, Dorn,

Table 2.2: Technical specifications of the detector array on CRIRES+

Detector Parameter	Value
type	H2RG
scale (pxiels)	6144 × 2048
pixel size (arc-second/pix)	0.059
read-out noise(e^-/pix)	6
dark current ($e^-/pix/s$)	3×10^{-3}
maximum extraction aperture (pixel)	35

Anglada-Escude, et al. 2014, Dorn, Bristow, et al. 2023). The updated instrument can cover six individual infrared bands (Y, J, K, H, L, M), and is able to achieve a high spectral resolution for over 100,000 by utilizing both cross-disperser and echelle gratings (shown in Fig. 2.2), which enhances its capabilities for studying the thermal emission from the atmosphere of hot giants with direct spectroscopy (Dorn, Anglada-Escude, et al. 2014). Moreover, the refurbished AO system MACAO is expected to significantly dampen the stellar light to retrieve the signals of spatially resolved planets.

In particular, the detector array consists of three Hawaii 2RG (H2RG) detectors with the size 2048 × 2048 pixels of each, thus 6144 × 2048 pixels in total. Each pixel has a physical size of 18 μm , corresponding to a projected angular size on sky of 0.059 arc-second. The read-out noise and dark current are considered as the noise contribution from instruments, which can be reduced to a lower level with the updated detector arrays to improve the SNR for detection of molecular emissions from the atmosphere of giant planets. The technical specifications of the detectors are presented in Table 2.2, and more information about CRIRES+ optical system can be found in Dorn, Anglada-Escude, et al. 2014 and presented on the science operation page of the instrument [CRIRES+](#).

2.3 Planet-to-star flux contrast

Planet-to-star flux contrast ratio (R) refers to the ratio of the light emitted or reflected by a planet orbiting around the host star to the light emitted by the star itself. Planet-to-star contrast is a fast and direct way to assess the possibility for planetary-signal detection, comparing with Cross-correlation Function (CCF) technique that will be discussed soon in Chapter 4.

In terms of non-transiting young planets embedded in protoplanetary disks, it is reasonable to assume a self-luminous regime due to the high effective temperature (>1000 K) to follow Equation 1.15. Since CRIRES+ is capable to spatially resolve the planet from the star as a separated source, we are able to locate both planet at $(x_{0,p})$, and the star at $(x_{0,*})$ on the detector plane. Assuming Point-Source Function (PSF) profiles are the same at a given order, two separated and equal PSF profiles must be considered on the detector plane, for the host star (P_*) and for the planet (P_p) respectively. Both profiles are supposed to reach equal peak value, i.e.:

$$P_p(\lambda, x_{0,p}) = P_*(\lambda, x_{0,*}) \quad (2.1)$$

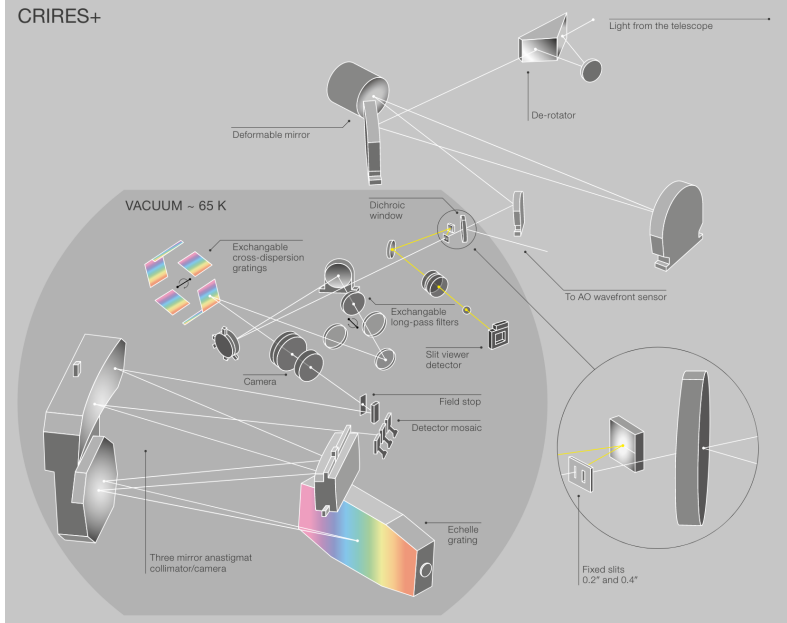


Figure 2.2: The optical design of the cross-dispersion pre-optics for CRIRRES+, from Arsenault et al. 2014

Considering the input SED spectrum s , PSF profile P , and the instrumental and atmospheric throughput T , assuming T is only dependent on wavelength, the flux distribution function of a source at a given spatial position $m(\lambda, x)$ can be described as

$$m(\lambda, x) = s(\lambda)P(\lambda, x)T(\lambda) \quad (2.2)$$

where λ corresponds to the wavelength and x corresponds to spatial axis (Kitchin 2021).

Therefore, from observation point of view, for a given λ , we can use the observed flux at the planet's position ($m(\lambda, x_p)$) and it at the host star's position $m(\lambda, x_*)$ to represent the intrinsic planet-to-star flux ratio as P and T eventually cancel out from the ratio formula. Thus equation 1.15 can be re-written as:

$$R = \frac{s_p(\lambda)}{s_*(\lambda)} = \frac{m_p(\lambda, x_{0,p})}{m_*(\lambda, x_{0,*})} = \frac{s_p(\lambda)P_p(\lambda, x_{0,p})T(\lambda)}{s_*(\lambda)P_*(\lambda, x_{0,*})T(\lambda)} \quad (2.3)$$

for a given wavelength λ . and inside the slit Because the planet is assumed to be spatially resolved from the star, which angular separation is larger than diffraction limit.

To better understand the feasibility of utilizing HDS observation, it is also worthwhile to compare the in-situ flux contrast ratio, namely the flux ratio between both objects at the exact position of planet ($x_{0,p}$), which is expected to be higher than the intrinsic one due to the dampened diffraction wing after AO correction:

$$R_{in-situ} = \frac{m_p(\lambda, x_{0,p})}{m_*(\lambda, x_{0,p})} = \frac{s_p(\lambda)P_p(\lambda, x_{0,p})T(\lambda)}{s_*(\lambda)P_*(\lambda, x_{0,p})T(\lambda)} = k \frac{s_p(\lambda)}{s_*(\lambda)} \quad (2.4)$$

where

$$k = \frac{P_p(\lambda, x_{0,p})}{P_*(\lambda, x_{0,p})} \quad (2.5)$$

Furthermore, for high-resolution spectroscopic observation of planets' atmosphere, we can calculate the SNR as:

$$\text{SNR}_{\text{planet}} = k \left(\frac{S_{\text{p}}}{S_{\star}} \right) \text{SNR}_{\text{star}} \sqrt{N_{\text{lines}}} \quad (2.6)$$

where N_{lines} is the number of lines detected at the planet's location in the observed wavelength range (Birkby 2018).

2.4 Pipeline to Produce Synthetic Observations

The primary goal of this simulation pipeline is to study the feasibility of high-dispersion spectroscopic (HDS) observations with CRILES+ for spatially resolved planets. By utilizing BT-Settl models for atmospheric SED of giant planets, it aims to re-construct the raw images, namely the dispersed signal on the detector plane, and then calculate the metrics to identify the most observationally favorable cases, such as planet-to-flux ratio, signal-to-noise ratio and other involved quantities that will be discussed later. By analyzing the difference of the quantities from different models, it aims to determine the feasibility of HDS observation for young planets in various configurations.

The Exposure Time Calculator (ETC) of CRILES+ developed by ESO ¹ is capable to generate synthetic observations from an uploaded spectrum. However, for spatially resolved planets, it is necessary to use the two-dimensional spectra, preserving the dispersion direction during the analysis. This feature is not included in the online ETC tool. As the planet is embedded in the diffracting light of the host star, to better understand the detectability, it is essential to re-construct the raw images of dispersing light on the detector plane from 1-D synthetic observations, in combination with several instrumental effects. The sketch of the pipeline's workflow is illustrated on Fig. 2.4.

2.4.1 ETC computation

The Exposure Time Calculator (ETC) for CRILES+ allows researchers to simulate the real observation results by inputting the SED of target and with various instrumental set-up, e.g. the exposure time and series, observation modes, Earth's atmospheric conditions, etc. We apply the ETC to the whole library of synthetic observations so that the results can be used to understand the feasibility of observation for planets under different physical configurations. Some important set-up are presented in Table 2.3.

In particular, for parameters related to the targets, we set the exposure time as 36 minutes in total (without overheads), which is similar to the CRILES+ observation for the ultra-hot transiting planet MASCARA 1-b that led to robust detection of CO, H₂O and Fe emission lines (Ramkumar et al. 2023). To avoid strong extinction from the disk and ISM and obtain a relatively higher planet-to-star contrast ratio, the observation is simulated in K-band with wavelength coverage from 1921.318 nm

¹<https://etc.eso.org/observing/etc/criles2>

Table 2.3: ETC Set-up

Atmosphere	Target		Seeing and Instruments		
air-mass	1.2	ref. wavelength	K2166	extraction aperture (pixel)	35 (star) 1-35 (planet)
FLI	0.5	brightness (K-band)	6.41 (star) 17.14 (planet)	turbulence	70%
PWV	2.5	NDIT \times DIT(s)	18 \times 120	slit width (arcsec)	0.2

Table 2.4: Wavelength coverage of K2166 setting

Order	$\lambda_{min}(\text{\AA})$	$\lambda_{max}(\text{\AA})$
29	19213.18	19611.28
28	19899.78	20311.65
27	20637.11	21063.92
26	21430.87	21873.86
25	22287.86	22748.35
24	23215.96	23695.34
23	24224.15	24723.88

to 2472.388 nm (the setting is named as K2166 as shown in Table 2.4) divided into 7 echelle orders (we hereafter refer to each of these as "orders"), which each is separated into 3 sub-orders for three detectors. The planet K-band magnitude is calculated assuming a planet-to-star contrast ratio of 5.1×10^{-5} . This is the 3 sigma upper limit to the planet-to-contrast ratio measured with VLT SPHERE. (Hammond et al. 2023)

As an example, the SED plotted in Fig.2.1 is processed by ETC with these set-up. The result spectrum is shown in Fig 2.3.

In addition, a few quantities are used to roughly control to atmospheric conditions during observation. Turbulence level is set up at 70% which corresponds to a seeing of ≤ 1.15 . FLI is fractional lunar illumination, which one represents full-moon and zero represents as moonless night. For simulation we set it as 0.5. PWV (predictable water vapor) is a quantity to measure the amount of water vapor lines in mm, which is set to 2.5(for more information, see the [CRIRES+ User Manual v2](#)).

2.4.2 Principles of the reconstruction of raw images

The detector plane can be defined as a 2-D plane formed by the horizontal dispersion axis which marks wavelength, and the vertical spatial axis which marks the angular separation between planet and the host star. Then, we try to re-construct the 2-D observed spectra, usually called raw images in real observation, starting from ETC which only provides the final 1-D extracted spectra that is actually a convolution of several components.

The extraction aperture refers to the size and shape of the region over which the light

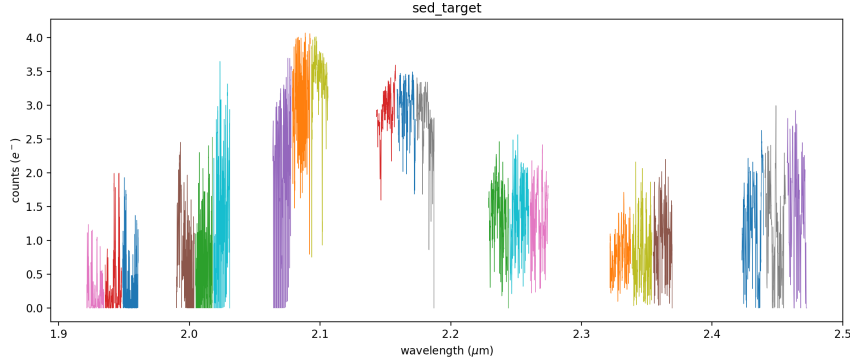


Figure 2.3: Example ETC simulated 1-dimensional simulated observation of a planet with $T_{eff}=1000\text{K}$, $\log(g)=4.0$, Metallicity=0.0, and instrumental and atmospheric set-up the same as Table 2.3. The whole spectrum is cut into 7 orders and 21 sub-orders denoted by different colors.

from the target is collected from raw images. It essentially defines the portion of the observed light that will contribute to the final spectrum. The extraction aperture can be expressed as a uniform window function A contributed to the equation 2.2. The flux distribution captured by the extraction aperture $f(\lambda, x)$ is :

$$\begin{aligned} f(\lambda, x) &= s(\lambda)P(\lambda, x)T(\lambda)A(x) \\ A(x) &= 1(0 \leq x \leq a) \end{aligned} \quad (2.7)$$

where a is the width of the extraction aperture. Therefore the observed 1-D spectrum can be expressed as the integral:

$$f(\lambda) = \int_{-\infty}^{\infty} f(\lambda, x)dx = \int_0^a m(\lambda, x)dx = s(\lambda)T(\lambda) \int_0^a P(\lambda, x)dx \quad (2.8)$$

It is clear that the spectrum is modified by the PSF pattern of the slit. Here we assume the instrumental and atmospheric throughput are only functions of wavelength.

ETC already includes the information on the PSF profile but only provided the extracted spectra under convolution. To re-construct the 2-D raw images, instead of considering a specific PSF profile, an alternative way is to vary the size of extraction aperture on ETC, and then make the difference of the 1-D spectra set with gradually ascending size of the extraction aperture ². If the central pixel of the aperture is denoted as 0, assuming the PSF profile is symmetric and the aperture size as a , then $f_a(\lambda)$, the convolved flux along the spatial axis can be derived as:

$$f_a(\lambda) = \int_{-n}^n m(\lambda, x)dx = s(\lambda)T(\lambda) \int_{-n}^n P(\lambda, x)dx, a = 2n + 1 (0 \leq n \leq 17, n \in \mathbb{Z}) \quad (2.9)$$

where n denotes the coordinate of pixel along the spatial axis, and $a = 1, 3, 5, \dots, 35$. Taking into account the detector plane as discrete pixels, the equation above can be

²The ETC tool for CRIRES+ may suffer from some problems to generate narrow PSF profiles and thus provide wrong results

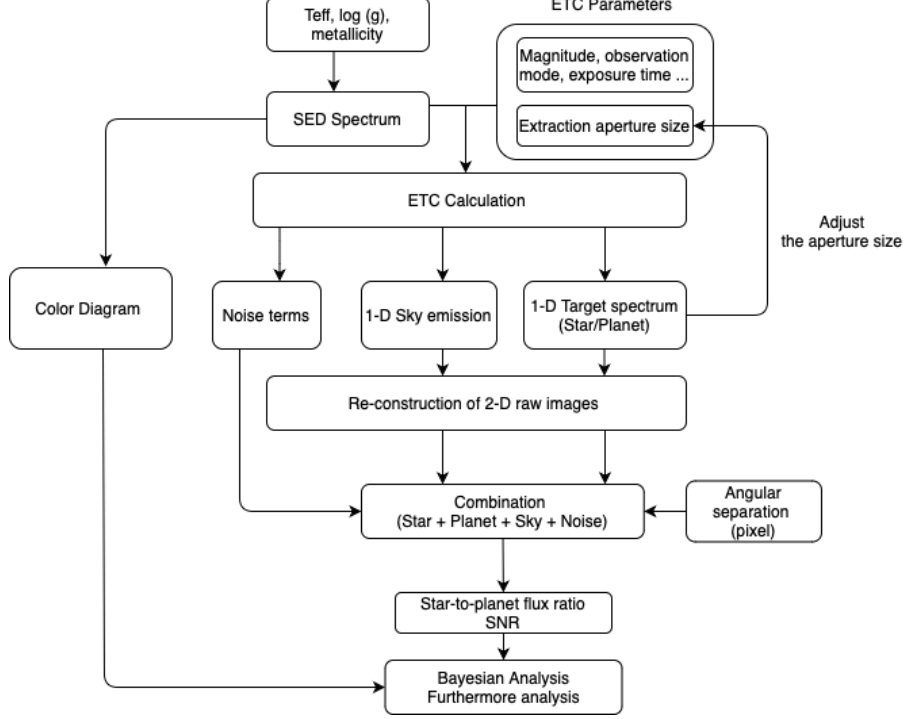


Figure 2.4: The workflow diagram of the simulation pipeline

adjusted from integral into summation:

$$f_a(\lambda) = \sum_{x=-n}^n m(\lambda, x) = s(\lambda)T(\lambda) \sum_{x=-n}^n P(\lambda, x)dx, a = 2n + 1 (0 \leq n \leq 17, n \in \mathbb{Z}) \quad (2.10)$$

Therefore, the flux at $(\lambda, \pm n)$, namely at a specific wavelength and a fixed pixel along spatial axis on the plane, can be retrieved by calculating the difference

$$f(\lambda, \pm n) = \frac{f_{a_i}(\lambda) - f_{a_{i-1}}(\lambda)}{2}, a = \{a_i\} = \{1, 3, 5, \dots, 35\} \quad (2.11)$$

2.5 Photometric system and color indexes

The apparent magnitude of planets can provide a direct information for the possibility of detection over different bands, while color index, as a quantity independent from distance (Gallaway 2020), is useful to indicate the intrinsic difference of atmospheric composition (F. Allard et al. 2012). Since we generate a series of simulated spectra under different configurations (different T_{eff} , $\log(g)$, Metallicity), it is a good way to compare their magnitudes, calculate color indexes and plot color diagrams to understand which configuration is more suitable for High-Dispersion Spectroscopy observation in the future.

To plot a color-Temperature or color-magnitude diagram, it is important to select a proper photometric system and retrieve the relative zero-point flux values. We follow the photometric system of Mauna Kea Observatory (MKO), with the transmission profiles and zero-point flux measured from the infrared camera NSFCam2

Table 2.5: Zero-Point Magnitude and Atmospheric Extinction Coefficients of J and K' band

	$\lambda_{min} - \lambda_{max}$ (\AA)	zero-point flux ($erg/cm^2/s/\text{\AA}$)
<i>J</i>	11481.78-13494.41	2.983e-10
<i>K_s</i>	19501.89-23377.11	4.364e-11

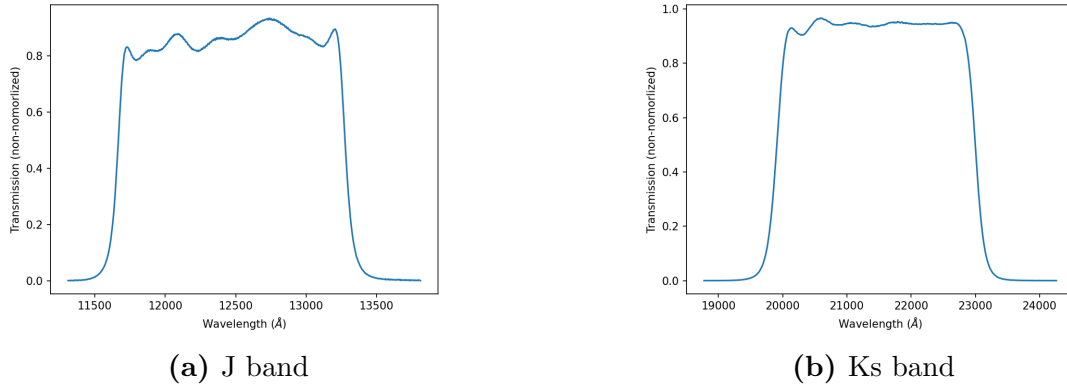


Figure 2.5: NSFCam2 transmission profiles in J and Ks band

utilizing the same type of detector as CRIRES+ (Shure et al. 1994)³. The transmission profiles are plotted in Fig. 2.5, and the zero-point flux F_0 for Vega are shown in Table 2.5.

Then, the magnitude can be calculated according to Pogson equation:

$$F = \frac{\int (f(\lambda) \cdot S(\lambda)) d\lambda}{\int S(\lambda) d\lambda} \quad (2.12)$$

$$M_{cal} = -2.5 * \log_{10} \frac{F}{F_0}$$

where $f(\lambda)$ corresponds to the flux density and $S(\lambda)$ corresponds to bandpass transmission profiles (Pickles et al. 2010, Bessell 2005, Gallaway 2020). The color index b between two bands can be calculated as

$$b = M_{cal,1} - M_{cal,2} \quad (2.13)$$

Notably, atmospheric extinction is ignored here since we focus on the theoretical magnitude of the planets.

³Official webpage: [NSFCam2](#)

Chapter 3

Results and Analysis

In this chapter we present the results of this thesis work. In Section 3.1, a set of models for HD 169142b is identified that are compatible with with the IFS observation in K band of this object. In Section 3.2 we present simulated observation of raw images for HD 169142b with CRIFRES+ based on one model that previously selected. Finally, in Section 3.3, a preliminary analysis is implemented to understand the sensitivity of CRIFRES+ on detection of HD 169142b’s atmospheric emission.

3.1 Color Diagram

With 55 simulated spectra for the planet’s atmospheric emission, we firstly make the color diagram to study the color dependence for simulated spectra in various configurations as well as computing the theoretical magnitude of the planet in Ks band. The color-Temperature tracks for different $\log(g)$ are shown in Fig. 3.1a. According to France Allard et al. 2001 and F. Allard et al. 2011, dust cloud formation is dominant for $T_{eff} < 2500K$ associated with greenhouse effect, leading to extremely red colors for late M and early L dwarfs comparing with Very-Low-Mass stars. However, when $T_{eff} < 1800K$, the greenhouse effect saturated and Methane (CH_4) clouds gradually forms in the condensation layers and make strong absorption at the peak of Ks band, which leads to a sharper transition towards bluer color indexes as demonstrated in 2.1, especially for the temperature of T dwarfs ($< 1300K$) which is consistent with the color analysis in Testi 2009. Surprisingly, as plotted in 3.1b, the track with $\log(g)=5.5$ matches very closely with a lower gravity setting, $\log(g)=4$ shown in Figure 4 in F. Allard et al. 2012, indicating a possible typo in F. Allard et al. 2012. Moreover, the gravity range of brown dwarf sample in Testi 2009 is $5.0 < \log(g) < 6.0$, which reproduces similar color changing as our results. Therefore, hereafter we concentrate on the examples with $\log(g) = 5.5$.

We also calculate the Ks magnitudes for planets ($M_{p,Ks}$) based on the stellar J magnitude ($M_{*,J}$), the J band planet-to-star contrast (R_J) and the calculated color index (b_{J-Ks}):

$$\begin{aligned} M_{p,J} &= M_{*,J} + \log_{10}(R_J) \\ M_{p,Ks} &= M_{p,J} - b_{J-Ks} \end{aligned} \tag{3.1}$$

Then $M_{p,Ks}$ is compared with the upper limit to the Ks band magnitude of HD 169142b as mentioned in Section 2.4. The uncertainty of calculation are propagated

from the uncertainty of flux contrast measurement in Table 1.2. As plotted in Fig. 3.2, for spectra with $\log(g) > 4.0$, the brightness at Ks band enhances with temperature increasing in general. However for those with $\log(g) < 4.0$, the brightness drops down with temperature increasing. And the color is much redder than other cases. The mechanism of this low-gravity reddening can be complicated, related to the dusty cloud formation scenario, which consider different condensing temperatures of multiple components in the atmosphere, and associated sink processes (Woitke et al. 2020). In addition, we found that for most settings the planet is brighter in Ks band than J band, the only models incompatible with IFS observations by Hammond et al. 2023 at K band is when $T_{eff} = 1700\text{K}$ for high gravity ($\log(g) = 5, 5.5$) and low gravity models cooler than 1600K .

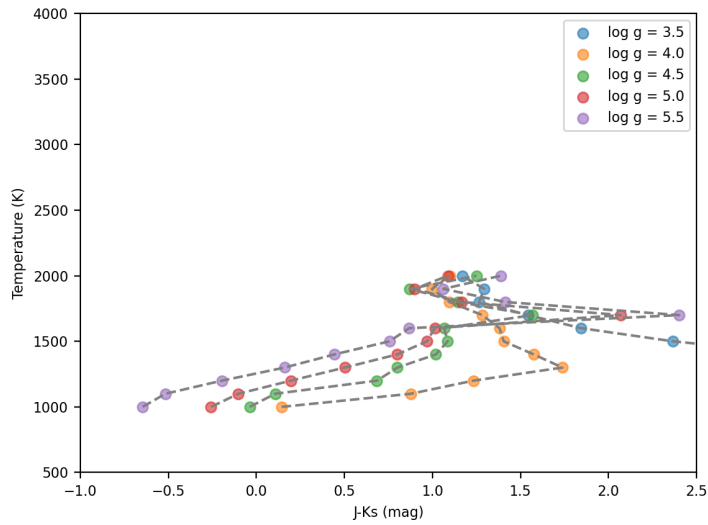
3.2 Reconstruction of Raw Images

An example of the 2-D raw image combining stellar light and planet signal is shown in Fig. 3.3 and Fig. 3.4. The planet is found at an angular separation of 6 arc-seconds, corresponding to 6 pixels, and is marked with horizontal dashed line in two figures mentioned above. Noise terms derived from the instrument and the sky contribution are also included. It is obvious that the dispersing light is strongly absorbed by the Earth's atmosphere in near-Infrared band, while less absorption contaminates on order-27 to order-24 that covers most CO emission lines (Birkby 2018). Therefore, it is feasible to observe potential CO lines from HD 169142b.

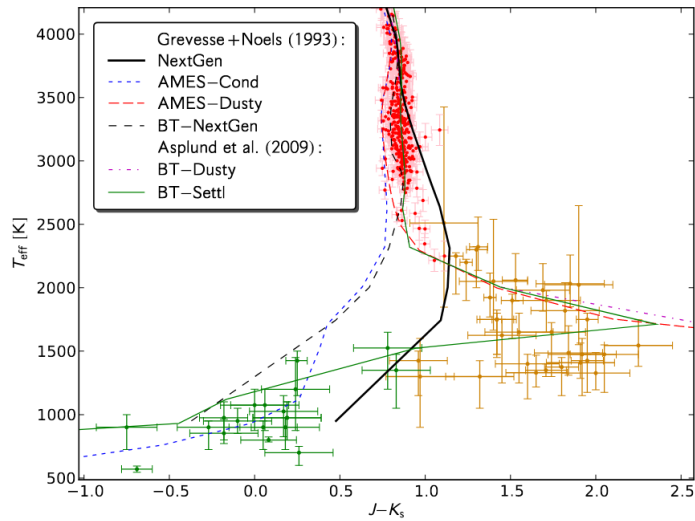
Additionally, as expected, it is difficult to immediately distinguish the planetary signal on the raw images even though the AO technique significantly dampens the PSF wings and spatially resolved two sources, which means the planetary signal is still embedded in the light from the host star due to its weak emission. Therefore, Bayesian techniques are required to boost the SNR with specially-designed cross-correlation functions (Brogi et al. 2019). It will be discussed later in Chapter 4.

3.3 Flux contrast

As mentioned in Snellen et al. 2015, the follow-up high-dispersion spectroscopy combined with AO is capable to separate the planet signal at a contrast of 10^{-7} , with a strehl ratio of 0.3 and a planet projection position at 0.6 pixel as shown in Fig 1.11. The effective temperature of the host star is more than 7000K corresponding to the black-body profile peak at $\lambda < 1 \mu\text{m}$, while the self-luminous planet with temperature from 1000 to 2000K reach its black-body emission peak at around 1.4 to $2.9 \mu\text{m}$, which is reasonable to obtain a contrast higher than 10^{-7} . To assess the improvement of sensitivity due to AO, we compare the intrinsic and in-situ planet-to-star flux contrast R and $R_{in-situ}$. In particular, $R_{in-situ}$ represents the contrast ratio measured at the spatially resolved planet location, and thus represents the contrast we need to reach with high dispersion spectroscopy to achieve a detection. As the contrast along dispersion axis shown in Fig 3.5 associated with the configuration $T_{eff} = 1300\text{K}$, $\log(g) = 5.5$, $Metallicity = 0.0$, both intrinsic (R) and in-situ ($R_{in-situ}$) contrast can reach over 10^{-5} and 10^{-3} respectively in our simulation. The



(a) The Color-Temperature diagram of BT-Settl generated spectra. The color indices are computed from $J - K_s$ as described in Section 2.5. Different gravity settings are denoted in different colors. In addition, we adjust the scales the same as Fig. 3.1b to make comparison easy.



(b) We focus on green lines that marks the simulation from BT-Settl fitting with an observed Brown Dwarf sample, with $\log(g) = 4.0$. Full explanation can be found in F. Allard et al. 2012.

Figure 3.1: Comparison of the Color-Temperature Diagram between the BT-Settl simulation from this work and F. Allard et al. 2012

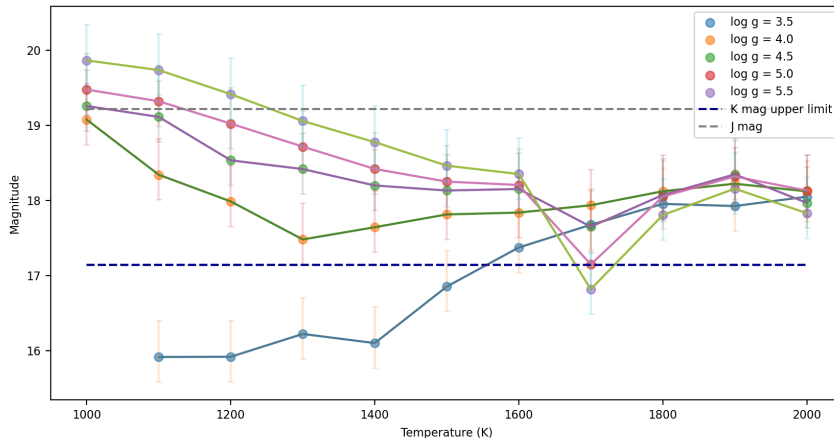


Figure 3.2: The Magnitude-Temperature diagram for Ks magnitude retrieved from models. The blue dashed line marks the Ks magnitude of the planet calculated from the non-detection limit of 5.1×10^{-5} . To compare the brightness in two bands, J magnitude retrieved from the observation by Hammond et al. 2023 ($M_{p,J}$) is also marked here as the gray dashed line.

AO significantly helps to reduce PSF wings and promotes the flux contrast of around 30 times higher at planet’s position than the intrinsic one. Additionally, it shows more than 30 times of fluctuation in order-29, which is probably due to the Earth’s atmospheric absorption similar to the results of 2-D raw images in Fig. 3.3. On the other hand, from order-27 to order-25 it shows stable contrast of $\log(R_{in-situ}) \geq -3$ over most wavelengths, which is consistent with what we see from raw images as mentioned before. It again indicates a high SNR observation in these orders.

Moreover, since the physical properties for HD 169142b are still mostly unconstrained by observations, it is worthwhile to figure out which configuration leads to better planet-to-star contrast to be observed. We therefore plot the contrast maps with effective temperature varying for fixed gravity, shown in Fig. 3.6 and Fig. 3.7. Generally, for fixed $\log(g)$, the overall contrast slightly increases with increasing temperature by up to $10^{-0.5}$, indicating that it is easier for CRIFRES+ to acquire high-significance observation when the planet’s atmosphere has high effective temperature. On the other hand, the overall contrast is lower for larger $\log(g)$. Moreover, for low-gravity configuration ($\log(g)=3.5$), the contrast is significantly higher than higher gravity configurations, for the explored temperature range from 1000 to 1800K.

Fig. 3.7 presents the case of high gravity setting, i.e. $\log(g)=5.5$. The contrast reaches maximum in most wavelengths when $T_{eff} = 1700\text{K}$. It is consistent with what we obtain on the $J - Ks$ color diagram (Fig. 3.1a): the reddening of color index is abruptly reversed from $T_{eff} = 1700\text{K}$ down to $T_{eff} = 1000\text{K}$, namely the configuration with $T_{eff} = 1700\text{K}$ reaches the reddest color in simulation for $\log(g) = 5.5$, which emission is concentrated on Ks band that promote the contrast to maximum. Overall, CRIFRES+ observation in K2166 setting is favorable for young planets with $T_{eff} > 1500\text{K}$, particularly for planets at around 1700K which keep extremely red color.

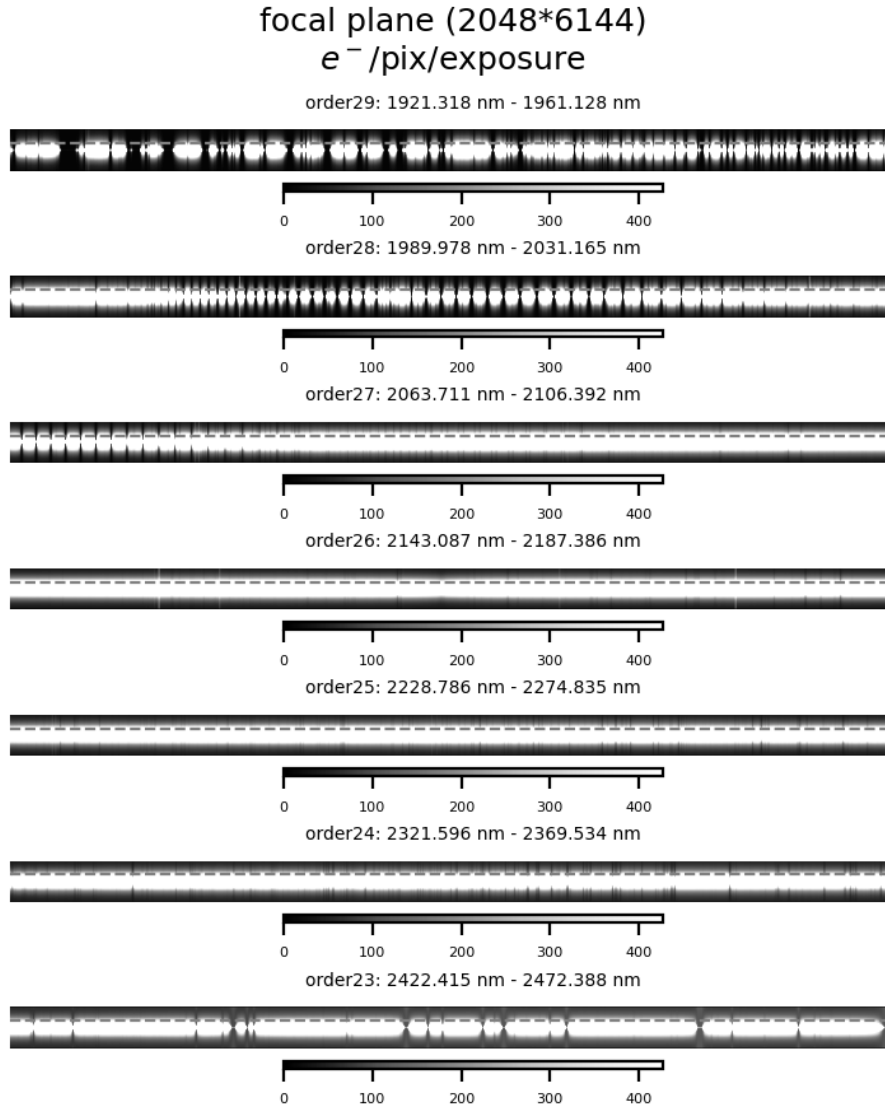


Figure 3.3: the 2-D raw image generated from the simulation pipeline for the 7 echelle orders in K2166 setting, associated with the simulation configuration $T_{eff} = 1300K$, $\log(g) = 5.5$, $Metallicity = 0.0$. The gray dashed line marks the projected position of the planet HD 169142b.

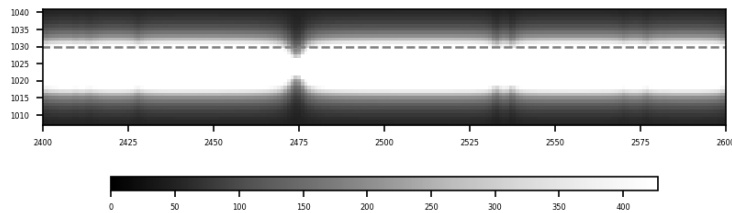


Figure 3.4: a zoom-in image on order-24 of Fig. 3.3 shown significant absorption due to the Earth's atmosphere

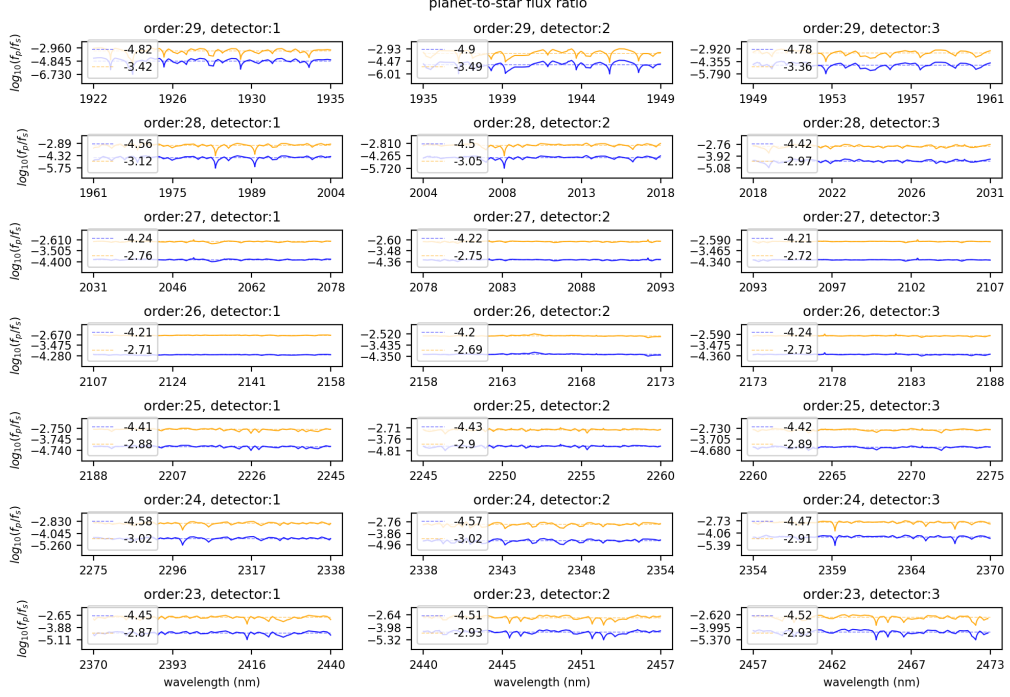


Figure 3.5: planet-to-star contrast ratio along wavelengths, for $T_{eff} = 1300K$, $\log(g) = 5.5$, $Metallicity = 0$. The blue line and yellow line marks intrinsic and in-situ planet-to-star contrast ratio, respectively, with the average value over the whole sub-order shown at lower-left.

Our results are comparable with CRIRES+ observation for the transiting planet MASCARA 1-b (Ramkumar et al. 2023), which contrast is $10^{-4} - 10^{-3}$ utilizing the CO emission-line template, which is even smaller than what we obtained in the most favorable cases as shown in Fig. 3.5. Hence, Our simulation support a high planet-to-star contrast ratio in real observation that CRIRES+ will be able to detect the atmosphere of HD 169142b in many cases.

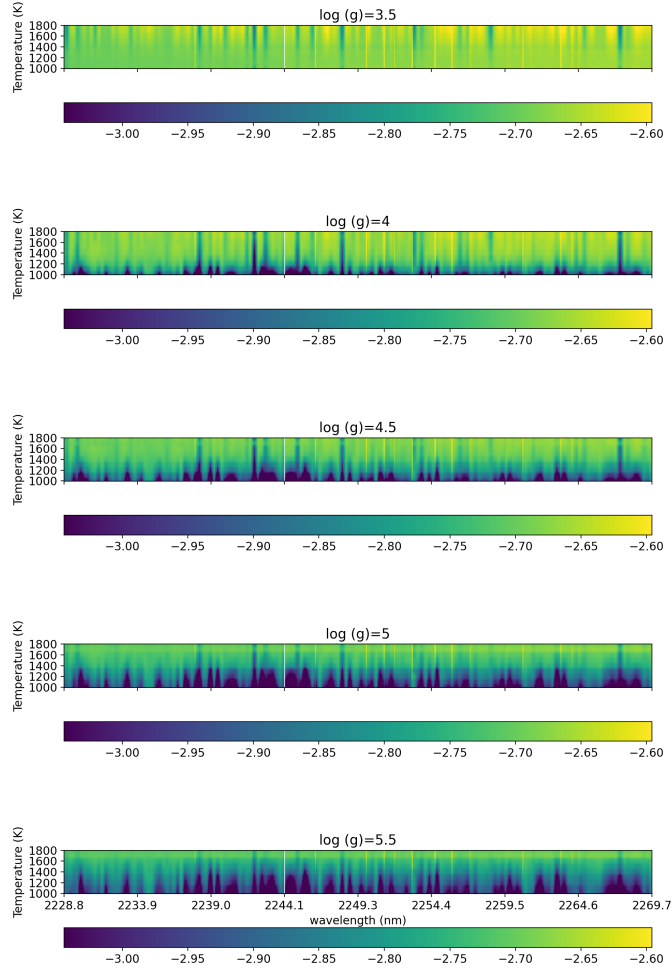


Figure 3.6: The $R_{in-situ}$ map given specific $\log(g)$. It is obvious that in general the contrast is higher when effective temperature increases, and when the surface gravity $\log(g)$ decreases, within a scale of $\Delta\log(R_{in-situ}) \sim 0.5$.

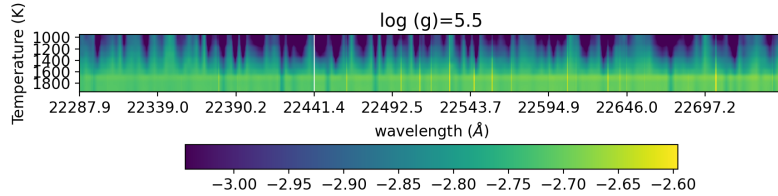


Figure 3.7: The map with $\log(g)=5.5$ in Fig. 3.6 from 1000 to 2000K, with y-axis upside down. It is clear that the contrast in 1700K is higher than it in other temperatures generally.

Chapter 4

Conclusion and Perspectives

4.1 Applying Novel Bayesian Framework

It is always challenging to convert cross-correlation values into a goodness-of-fit estimator to retrieve the physical properties of atmosphere. This is however a necessary step to quantify the properties of the studied atmospheres, e.g. the abundance of species.

For High-resolution Spectroscopy such as CRIRES+ observation, wavelength shift must be considered, therefore the log likelihood function L of cross-correlation (C) can be expressed as:

$$\begin{aligned} f(n) &= ag(n - s) + d_n \\ L &= \prod_n \frac{1}{\sqrt{2\pi\sigma^2}} \exp \left\{ -\frac{[f(n) - ag(n - s)]^2}{2\sigma^2} \right\} \\ &= \left(\frac{1}{\sqrt{2\pi\sigma^2}} \right)^N \exp \left\{ -\sum_n \frac{[f(n) - ag(n - s)]^2}{2\sigma^2} \right\} \end{aligned} \quad (4.1)$$

where $f(n)$ is a single observed spectrum and $g(n)$ is a template spectrum. Both $f(n)$ and $g(n)$ are continuum-extracted for determination of emission-line significance. Then, n represents the bin number or spectral channel, then a denotes a scaling factor, s denotes wavelength shift and d_n is the noise at bin n . The noise is assumed to be Gaussian-distributed at each pixel with standard deviation σ .

Hence the log likelihood function is:

$$\log(L) = -N \log \sigma - \frac{1}{2\sigma^2} \sum_n [f(n) - ag(n - s)]^2 \quad (4.2)$$

with this new formula, Brogi et al. 2019 designed a new Bayesian approach for High Resolution Cross-correlation Spectroscopy (HRCCS) as plotted in Fig. 4.1. In the next step, this framework will be implemented into our pipeline to analyze the significance of various molecular signals in synthetic observation, for the library of spectra. We aim to figure out the feasibility of molecular-line detection and characterization on young planets in different effective temperatures, gravity and metal abundances.

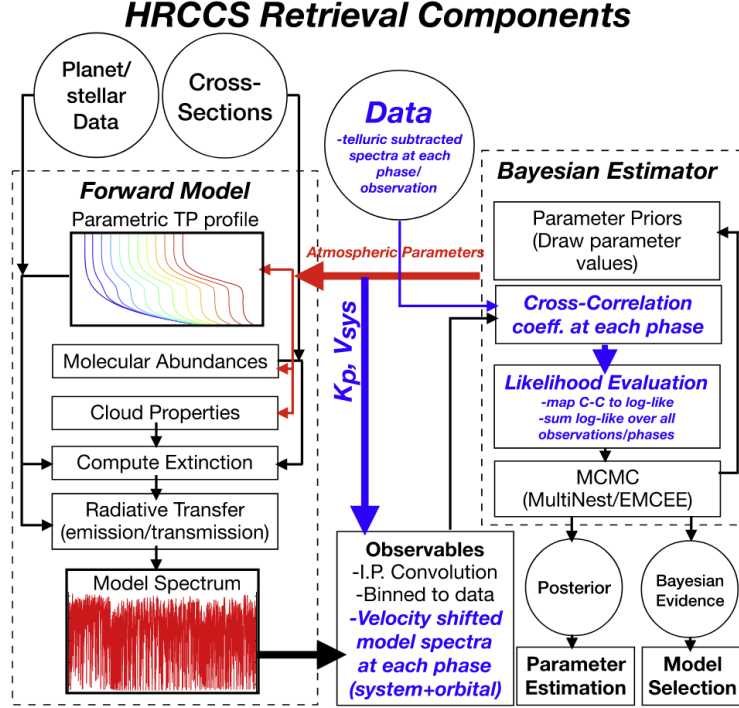


Figure 4.1: The workflow of HRCCS to retrieve planetary parameters, from Brogi et al. 2019

4.2 Future Instruments

Extremely Large Telescope (ELT) is the next-generation ground-based telescope and will be installed with the largest 39m main-mirror diameter. Two main instruments are expected to engage in HCI+HDS observation. the extremely high dispersion spectrometer ANDES and mid-infrared imager METIS (Marconi et al. 2022, Blain et al. 2022). ANDES is capable to reach the resolution of 100,000 with default ELT Adaptive Optics, enables the precise and direct spectroscopy for diverse types of exoplanets to understand their chemical compositions and weather in atmospheres, and search for bio-signatures from atmospheric emission. METIS covers a wide wavelength range from 3 to 13 μm and carries advanced coronagraphy and AO system. It allows a stronger capability of planet detection over a large range of effective temperatures, and the integral field Spectroscopy at L/M band with a resolution of 1,000 enables a higher precision for separation measurement.

Our study is a pathfinder for atmospheric characterization of exoplanets using ELT. The pipeline of synthetic spectra can be adjusted to work with ETC of ANDES, therefore it can help astronomers to better understand the detection of exoplanet observation in the era of ELT. Moreover, the feasibility study of several young planets with current instrument CRIRES+ can inspire the astronomers to make a reliable list of interesting targets for METIS observation.

4.3 Conclusion

We selected the BT-Settl models that are compatible with current observations on target planet HD 169142b. And next we generated a library of synthetic observations through a specially-designed pipeline to obtain the 2-D observed spectra (“Raw images”) associated with CRIRES+ on VLT. To make a preliminary assessment on the feasibility of CRIRES+ observations for the planet, we computed the planet-to-star flux contrast ratio based on the 2-D observed spectra, and tried to understand the telluric contamination along different orders by checking the simulated raw images. Moreover, Using the selected BT-Settl models, we produced the Color-Temperature and Color-Magnitude diagram, to retrieve the theoretical magnitude at specific bands and understand the color dependence of HD 169142b.

From color analysis, the models with $\log(g)=5.5$ are more compatible with previous observations, and the retrieved magnitude at Ks band provide an estimation of planet’s magnitude under various different physical configurations, and therefore could be informative for observation proposals on HD 169142 planetary system. Additionally, low-gravity models present opposite behaviors on Color-Magnitude and Color-Temperature diagrams. It is worthwhile to explore the intrinsic mechanism in future study.

Concentrating on the target planetary system HD 169142, we conclude that for $\log(g) = 5.5$, in the temperature range 1000-2000 K it shows a high planet-to-flux contrast over 10^{-3} at the position of planet, with around 2 orders of improvement from the intrinsic planet-to-star contrast. It thus supports a strong detectability for HD 169142b. More generally, CRIRES+ is favorable to high effective temperature scenarios which $T_{eff} > 1500\text{K}$. In addition, by checking the re-constructed raw images, we found that from order-27 to order-24 the spectrum is less absorbed by the Earth’s atmosphere, which makes these orders the most favorable for detection of the planet’s atmosphere.

In the next step, Bayesian analysis will be implemented on the 2-D observed spectra in order to analyze the significance of various molecular lines in a more quantitative way. The novel Bayesian framework for HRCCS will also be applied and tested. We will optimize the pipeline to be more flexible to work with ETC tool from different telescopes such as next-generation HDS instrument ANDES. Hence, it can be utilized to pathfinder research for ANDES observation that focuses on young planet characterization in the next decades.

Bibliography

- Lyot, Bernard (June 1939). “The study of the solar corona and prominences without eclipses (George Darwin Lecture, 1939)”. In: 99, p. 580. DOI: [10.1093/mnras/99.8.580](https://doi.org/10.1093/mnras/99.8.580).
- Perri, F. and A. G. W. Cameron (Aug. 1974). “Hydrodynamic Instability of the Solar Nebula in the Presence of a Planetary Core”. In: 22.4, pp. 416–425. DOI: [10.1016/0019-1035\(74\)90074-8](https://doi.org/10.1016/0019-1035(74)90074-8).
- Mizuno, H. (Aug. 1980). “Formation of the Giant Planets”. In: *Progress of Theoretical Physics* 64.2, pp. 544–557. DOI: [10.1143/PTP.64.544](https://doi.org/10.1143/PTP.64.544).
- Goodman, A. A. et al. (Apr. 1993). “Dense Cores in Dark Clouds. VIII. Velocity Gradients”. In: 406, p. 528. DOI: [10.1086/172465](https://doi.org/10.1086/172465).
- Shure, Mark A. et al. (June 1994). “NSFCAM: a new infrared array camera for the NASA Infrared Telescope Facility”. In: *Instrumentation in Astronomy VIII*. Ed. by David L. Crawford and Eric R. Craine. Vol. 2198. Society of Photo-Optical Instrumentation Engineers (SPIE) Conference Series, pp. 614–622. DOI: [10.1117/12.176769](https://doi.org/10.1117/12.176769).
- Mayor, Michel and Didier Queloz (Nov. 1995). “A Jupiter-mass companion to a solar-type star”. In: 378.6555, pp. 355–359. DOI: [10.1038/378355a0](https://doi.org/10.1038/378355a0).
- Pollack, James B. et al. (Nov. 1996). “Formation of the Giant Planets by Concurrent Accretion of Solids and Gas”. In: 124.1, pp. 62–85. DOI: [10.1006/icar.1996.0190](https://doi.org/10.1006/icar.1996.0190).
- Burrows, A. et al. (June 1997). “Advances in the Theory of Extrasolar Giant Planets and Brown Dwarfs”. In: *arXiv e-prints*, astro-ph/9706080, astro-ph/9706080. DOI: [10.48550/arXiv.astro-ph/9706080](https://doi.org/10.48550/arXiv.astro-ph/9706080). arXiv: [astro-ph/9706080](https://arxiv.org/abs/astro-ph/9706080) [[astro-ph](https://arxiv.org/abs/astro-ph/9706080)].
- Hubbard, W. B., T. Guillot, et al. (Oct. 1999). “Comparative evolution of Jupiter and Saturn”. In: 47.10-11, pp. 1175–1182. DOI: [10.1016/S0032-0633\(99\)00042-2](https://doi.org/10.1016/S0032-0633(99)00042-2). arXiv: [astro-ph/9812192](https://arxiv.org/abs/astro-ph/9812192) [[astro-ph](https://arxiv.org/abs/astro-ph/9812192)].
- Allard, France et al. (July 2001). “The Limiting Effects of Dust in Brown Dwarf Model Atmospheres”. en. In: *The Astrophysical Journal* 556.1, pp. 357–372. ISSN: 0004-637X, 1538-4357. DOI: [10.1086/321547](https://doi.org/10.1086/321547).
- Haisch Jr., Karl E., Elizabeth A. Lada, and Charles J. Lada (June 2001). “Disk Frequencies and Lifetimes in Young Clusters”. In: *The Astrophysical Journal* 553.2. arXiv:astro-ph/0104347, pp. L153–L156. ISSN: 0004637X. DOI: [10.1086/320685](https://doi.org/10.1086/320685).
- Sivaramakrishnan, Anand et al. (May 2001). “Ground-based Coronagraphy with High-order Adaptive Optics”. In: 552.1, pp. 397–408. DOI: [10.1086/320444](https://doi.org/10.1086/320444). arXiv: [astro-ph/0103012](https://arxiv.org/abs/astro-ph/0103012) [[astro-ph](https://arxiv.org/abs/astro-ph/0103012)].
- Hubbard, W. B., A. Burrows, and J. I. Lunine (Jan. 2002). “Theory of Giant Planets”. In: 40, pp. 103–136. DOI: [10.1146/annurev.astro.40.060401.093917](https://doi.org/10.1146/annurev.astro.40.060401.093917).

- Zucker, S. (July 2003). “Cross-correlation and maximum-likelihood analysis: a new approach to combining cross-correlation functions”. In: 342.4, pp. 1291–1298. DOI: [10.1046/j.1365-8711.2003.06633.x](https://doi.org/10.1046/j.1365-8711.2003.06633.x). arXiv: [astro-ph/0303426](https://arxiv.org/abs/astro-ph/0303426) [[astro-ph](#)].
- Kaeuffl, Hans-Ulrich et al. (Sept. 2004). “CRIRES: a high-resolution infrared spectrograph for ESO’s VLT”. In: *Ground-based Instrumentation for Astronomy*. Ed. by Alan F. M. Moorwood and Masanori Iye. Vol. 5492. Society of Photo-Optical Instrumentation Engineers (SPIE) Conference Series, pp. 1218–1227. DOI: [10.1117/12.551480](https://doi.org/10.1117/12.551480).
- Paardekooper, S.-J. and G. Mellema (Oct. 2004). “Planets opening dust gaps in gas disks”. en. In: *Astronomy Astrophysics* 425.1, pp. L9–L12. ISSN: 0004-6361, 1432-0746. DOI: [10.1051/0004-6361:200400053](https://doi.org/10.1051/0004-6361:200400053).
- Bessell, Michael S. (Sept. 2005). “Standard Photometric Systems”. en. In: *Annual Review of Astronomy and Astrophysics* 43.1, pp. 293–336. ISSN: 0066-4146, 1545-4282. DOI: [10.1146/annurev.astro.41.082801.100251](https://doi.org/10.1146/annurev.astro.41.082801.100251).
- Barber, R. J. et al. (May 2006). “A high-accuracy computed water line list”. In: 368.3, pp. 1087–1094. DOI: [10.1111/j.1365-2966.2006.10184.x](https://doi.org/10.1111/j.1365-2966.2006.10184.x). arXiv: [astro-ph/0601236](https://arxiv.org/abs/astro-ph/0601236) [[astro-ph](#)].
- Binney, James and Scott Tremaine (2008). *Galactic Dynamics: Second Edition*.
- Charbonnel, C, F Combes, and R Samadi (2008). “THE TIMESCALE FOR GIANT PLANET FORMATION: CONSTRAINTS FROM THE ROTATIONAL EVOLUTION OF EXOPLANET HOST STARS”. en. In.
- Claudi, R. U. et al. (July 2008). “SPHERE IFS: the spectro differential imager of the VLT for exoplanets search”. In: *Ground-based and Airborne Instrumentation for Astronomy II*. Ed. by Ian S. McLean and Mark M. Casali. Vol. 7014. Society of Photo-Optical Instrumentation Engineers (SPIE) Conference Series, 70143E, 70143E. DOI: [10.1117/12.788366](https://doi.org/10.1117/12.788366).
- Gustafsson, B. et al. (Aug. 2008). “A grid of MARCS model atmospheres for late-type stars. I. Methods and general properties”. In: 486.3, pp. 951–970. DOI: [10.1051/0004-6361:200809724](https://doi.org/10.1051/0004-6361:200809724). arXiv: [0805.0554](https://arxiv.org/abs/0805.0554) [[astro-ph](#)].
- Kalas, Paul et al. (Nov. 2008). “Optical Images of an Exosolar Planet 25 Light-Years from Earth”. In: *Science* 322.5906, p. 1345. DOI: [10.1126/science.1166609](https://doi.org/10.1126/science.1166609). arXiv: [0811.1994](https://arxiv.org/abs/0811.1994) [[astro-ph](#)].
- Tanigawa, Takayuki and K. Ohtsuki (May 2008). “Accretion Rates of Planetesimals by a Protoplanet Embedded in Nebular Gas”. In: *AAS/Division of Dynamical Astronomy Meeting #39*. Vol. 39. AAS/Division of Dynamical Astronomy Meeting, 15.10, p. 15.10.
- Testi, L. (Aug. 2009). “A low-resolution near-infrared spectral library of M-, L-, and T-dwarfs”. en. In: *Astronomy Astrophysics* 503.2, pp. 639–650. ISSN: 0004-6361, 1432-0746. DOI: [10.1051/0004-6361/200810699](https://doi.org/10.1051/0004-6361/200810699).
- Pickles, A and É Depagne (2010). “All-Sky Spectrally Matched UBVRi À ZY and u0g0r0i0z0 Magnitudes for Stars in the Tycho2 Catalog”. en. In.
- Seager, Sara and Drake Deming (Aug. 2010). “Exoplanet Atmospheres”. en. In: *Annual Review of Astronomy and Astrophysics* 48.1, pp. 631–672. ISSN: 0066-4146, 1545-4282. DOI: [10.1146/annurev-astro-081309-130837](https://doi.org/10.1146/annurev-astro-081309-130837).
- Allard, F., D. Homeier, and B. Freytag (Dec. 2011). “Model Atmospheres From Very Low Mass Stars to Brown Dwarfs”. In: *16th Cambridge Workshop on Cool*

- Stars, Stellar Systems, and the Sun*. Ed. by Christopher Johns-Krull, Matthew K. Browning, and Andrew A. West. Vol. 448. Astronomical Society of the Pacific Conference Series, p. 91. DOI: [10.48550/arXiv.1011.5405](https://doi.org/10.48550/arXiv.1011.5405). arXiv: [1011.5405](https://arxiv.org/abs/1011.5405) [astro-ph.SR].
- Dawson, Rebekah I., Ruth A. Murray-Clay, and Daniel C. Fabrycky (Dec. 2011). “On the Misalignment of the Directly Imaged Planet β Pictoris b with the System’s Warped Inner Disk”. In: 743.1, L17, p. L17. DOI: [10.1088/2041-8205/743/1/L17](https://doi.org/10.1088/2041-8205/743/1/L17). arXiv: [1111.0297](https://arxiv.org/abs/1111.0297) [astro-ph.EP].
- Williams, Jonathan P. and Lucas A. Cieza (Sept. 2011). “Protoplanetary Disks and Their Evolution”. en. In: *Annual Review of Astronomy and Astrophysics* 49.1. arXiv:1103.0556 [astro-ph], pp. 67–117. ISSN: 0066-4146, 1545-4282. DOI: [10.1146/annurev-astro-081710-102548](https://doi.org/10.1146/annurev-astro-081710-102548).
- Allard, F., D. Homeier, and B. Freytag (June 2012). “Models of very-low-mass stars, brown dwarfs and exoplanets”. In: *Philosophical Transactions of the Royal Society of London Series A* 370.1968, pp. 2765–2777. DOI: [10.1098/rsta.2011.0269](https://doi.org/10.1098/rsta.2011.0269). arXiv: [1112.3591](https://arxiv.org/abs/1112.3591) [astro-ph.SR].
- Davies, Richard and Markus Kasper (Sept. 2012). “Adaptive Optics for Astronomy”. In: 50, pp. 305–351. DOI: [10.1146/annurev-astro-081811-125447](https://doi.org/10.1146/annurev-astro-081811-125447). arXiv: [1201.5741](https://arxiv.org/abs/1201.5741) [astro-ph.IM].
- Armitage, Philip J. (2013). *Astrophysics of Planet Formation*.
- Quanz, Sascha P. et al. (Feb. 2013). “GAPS IN THE HD 169142 PROTOPLANETARY DISK REVEALED BY POLARIMETRIC IMAGING: SIGNS OF ONGOING PLANET FORMATION?” en. In: *The Astrophysical Journal* 766.1, p. L2. ISSN: 2041-8205, 2041-8213. DOI: [10.1088/2041-8205/766/1/L2](https://doi.org/10.1088/2041-8205/766/1/L2).
- Arsenault, Robin et al. (2014). “The Adaptive Optics Facility Module GRAAL on its Way to Final Validation”. en. In.
- Dorn, R. J., G. Anglada-Escude, et al. (June 2014). “CRIRES+: Exploring the Cold Universe at High Spectral Resolution”. In: *The Messenger* 156, pp. 7–11.
- Lockwood, Alexandra C. et al. (Mar. 2014). “Near-IR Direct Detection of Water Vapor in Tau Boötis b”. In: 783.2, L29, p. L29. DOI: [10.1088/2041-8205/783/2/L29](https://doi.org/10.1088/2041-8205/783/2/L29). arXiv: [1402.0846](https://arxiv.org/abs/1402.0846) [astro-ph.EP].
- Snellen, I. et al. (Apr. 2015). “Combining high-dispersion spectroscopy with high contrast imaging: Probing rocky planets around our nearest neighbors”. en. In: *Astronomy Astrophysics* 576, A59. ISSN: 0004-6361, 1432-0746. DOI: [10.1051/0004-6361/201425018](https://doi.org/10.1051/0004-6361/201425018).
- Andrews, S. M. et al. (Dec. 2018). “ALMA Observations of the Epoch of Planet Formation”. In: *The Messenger* 174, pp. 19–23. DOI: [10.18727/0722-6691/5108](https://doi.org/10.18727/0722-6691/5108).
- Ansdell, M. et al. (May 2018). “ALMA Survey of Lupus Protoplanetary Disks. II. Gas Disk Radii”. In: 859.1, 21, p. 21. DOI: [10.3847/1538-4357/aab890](https://doi.org/10.3847/1538-4357/aab890). arXiv: [1803.05923](https://arxiv.org/abs/1803.05923) [astro-ph.EP].
- Birkby, J. L. (June 2018). “Exoplanet Atmospheres at High Spectral Resolution”. en. In: arXiv:1806.04617. arXiv:1806.04617 [astro-ph]. URL: <http://arxiv.org/abs/1806.04617>.
- Dawson, Rebekah I. and John Asher Johnson (Sept. 2018). “Origins of Hot Jupiters”. en. In: *Annual Review of Astronomy and Astrophysics* 56.1, pp. 175–221. ISSN: 0066-4146, 1545-4282. DOI: [10.1146/annurev-astro-081817-051853](https://doi.org/10.1146/annurev-astro-081817-051853).

- Perryman, Michael (2018). *The Exoplanet Handbook*.
- Armitage, Philip J. and Wilhelm Kley (2019). *From Protoplanetary Disks to Planet Formation*. DOI: [10.1007/978-3-662-58687-7](https://doi.org/10.1007/978-3-662-58687-7).
- Beuzit, J. -L. et al. (Nov. 2019). “SPHERE: the exoplanet imager for the Very Large Telescope”. In: 631, A155, A155. DOI: [10.1051/0004-6361/201935251](https://doi.org/10.1051/0004-6361/201935251). arXiv: [1902.04080](https://arxiv.org/abs/1902.04080) [astro-ph.IM].
- Brogi, Matteo and Michael R. Line (Feb. 2019). “Retrieving Temperatures and Abundances of Exoplanet Atmospheres with High-resolution Cross-correlation Spectroscopy”. en. In: *The Astronomical Journal* 157.3, p. 114. ISSN: 1538-3881. DOI: [10.3847/1538-3881/aaffd3](https://doi.org/10.3847/1538-3881/aaffd3).
- Mesa, D. et al. (Dec. 2019). “VLT/SPHERE exploration of the young multiplanetary system PDS70”. en. In: *Astronomy Astrophysics* 632, A25. ISSN: 0004-6361, 1432-0746. DOI: [10.1051/0004-6361/201936764](https://doi.org/10.1051/0004-6361/201936764).
- Pinte, C. et al. (Aug. 2019). “Kinematic detection of a planet carving a gap in a protoplanetary disk”. In: *Nature Astronomy* 3, pp. 1109–1114. DOI: [10.1038/s41550-019-0852-6](https://doi.org/10.1038/s41550-019-0852-6). arXiv: [1907.02538](https://arxiv.org/abs/1907.02538) [astro-ph.SR].
- Zeng, Li et al. (May 2019). “Growth model interpretation of planet size distribution”. In: *Proceedings of the National Academy of Science* 116.20, pp. 9723–9728. DOI: [10.1073/pnas.1812905116](https://doi.org/10.1073/pnas.1812905116). arXiv: [1906.04253](https://arxiv.org/abs/1906.04253) [astro-ph.EP].
- Boccaletti, A. et al. (May 2020). “Possible evidence of ongoing planet formation in AB Aurigae. A showcase of the SPHERE/ALMA synergy”. In: 637, L5, p. L5. DOI: [10.1051/0004-6361/202038008](https://doi.org/10.1051/0004-6361/202038008). arXiv: [2005.09064](https://arxiv.org/abs/2005.09064) [astro-ph.EP].
- Gallaway, Mark (2020). *An Introduction to Observational Astrophysics*. en. Undergraduate Lecture Notes in Physics. Cham: Springer International Publishing. ISBN: 978-3-030-43550-9. DOI: [10.1007/978-3-030-43551-6](https://doi.org/10.1007/978-3-030-43551-6). URL: <http://link.springer.com/10.1007/978-3-030-43551-6>.
- Woitke, Peter, Christiane Helling, and Ophelia Gunn (Feb. 2020). “Dust in brown dwarfs and extra-solar planets: VII. Cloud formation in diffusive atmospheres”. en. In: *Astronomy Astrophysics* 634, A23. ISSN: 0004-6361, 1432-0746. DOI: [10.1051/0004-6361/201936281](https://doi.org/10.1051/0004-6361/201936281).
- Kitchin, C. R. (2021). *Astrophysical techniques*. en. 7th ed. Boca Raton: CRC press. ISBN: 978-1-138-59016-8.
- Saffe, C. et al. (Mar. 2021). “Chemical analysis of early-type stars with planets”. en. In: *Astronomy Astrophysics* 647, A49. ISSN: 0004-6361, 1432-0746. DOI: [10.1051/0004-6361/202040132](https://doi.org/10.1051/0004-6361/202040132).
- Wang, J. J. et al. (Mar. 2021). “Constraining the Nature of the PDS 70 Protoplanets with VLTI/GRAVITY”. en. In: *The Astronomical Journal* 161.3, p. 148. ISSN: 0004-6256, 1538-3881. DOI: [10.3847/1538-3881/abdb2d](https://doi.org/10.3847/1538-3881/abdb2d).
- Zhu, Wei and Subo Dong (Sept. 2021). “Exoplanet Statistics and Theoretical Implications”. en. In: *Annual Review of Astronomy and Astrophysics* 59.1, pp. 291–336. ISSN: 0066-4146, 1545-4282. DOI: [10.1146/annurev-astro-112420-020055](https://doi.org/10.1146/annurev-astro-112420-020055).
- Blain, Doriann et al. (Sept. 2022). “ELT-METIS: estimating the constraining power of high-resolution exoplanet spectra with Bayesian inference”. In: *European Planetary Science Congress, EPSC2022-484, EPSC2022-484*. DOI: [10.5194/epsc2022-484](https://doi.org/10.5194/epsc2022-484).

- Marconi, A. et al. (Aug. 2022). “ANDES, the high resolution spectrograph for the ELT: science case, baseline design and path to construction”. In: *Ground-based and Airborne Instrumentation for Astronomy IX*. Ed. by Christopher J. Evans, Julia J. Bryant, and Kentaro Motohara. Vol. 12184. Society of Photo-Optical Instrumentation Engineers (SPIE) Conference Series, 1218424, p. 1218424. DOI: [10.1117/12.2628689](https://doi.org/10.1117/12.2628689).
- Dorn, R. J., P. Bristow, et al. (Mar. 2023). “CRIRES⁺ on sky at the ESO Very Large Telescope. Observing the Universe at infrared wavelengths and high spectral resolution”. In: 671, A24, A24. DOI: [10.1051/0004-6361/202245217](https://doi.org/10.1051/0004-6361/202245217).
- Hammond, Iain et al. (Mar. 2023). “Confirmation and Keplerian motion of the gap-carving protoplanet HD 169142 b”. en. In: *Monthly Notices of the Royal Astronomical Society: Letters* 522.1, pp. L51–L55. ISSN: 1745-3925, 1745-3933. DOI: [10.1093/mnrasl/slad027](https://doi.org/10.1093/mnrasl/slad027).
- Ramkumar, Swaetha et al. (Oct. 2023). “High-resolution emission spectroscopy retrievals of MASCARA-1b with CRIRES+: strong detections of CO, H₂O, and Fe emission lines and a C/O consistent with solar”. In: 525.2, pp. 2985–3005. DOI: [10.1093/mnras/stad2476](https://doi.org/10.1093/mnras/stad2476). arXiv: [2308.07157](https://arxiv.org/abs/2308.07157) [astro-ph.EP].
- Stasevic, S. et al. (Oct. 2023). “An inner warp discovered in the disk around HD 110058 using VLT/SPHERE and HST/STIS”. In: 678, A8, A8. DOI: [10.1051/0004-6361/202346720](https://doi.org/10.1051/0004-6361/202346720). arXiv: [2308.05613](https://arxiv.org/abs/2308.05613) [astro-ph.EP].

Acknowledgement

On the occasion of my second anniversary in Italy for pursuing my studies, I have successfully completed my master's thesis. Crossing 7,000 kilometers to study in a completely different environment, I never felt alone or helpless. On the contrary, every day in Bologna was filled with the support of friends, the encouragement of professors, and the indulgence of gelato for my stomach. Through 730 days of up and down, I persevered steadfastly - from the primordial inflation of the universe to the formation of exoplanets, from struggling with ancient software (IRAF) to marvelling at Bayesian statistics. I passed from the summer mornings in Trento, the tranquil waves of Lake Garda, to the fields of spring in the glow of sunset in Val d'Orcia, and the fireworks on the rocky beaches of Monopoli, eventually back to the bustling Piazza Verdi on winter nights that felt like summer.

In the first half of 2023, my life became a strange tale full of movie moments. Permessso di soggiorno was stolen, phone was stolen, even bike seat was stolen. Hit by a motorcycle, I took an 11-hour Flixbus journey from Geneva back to Bologna, undergoing surgery with a clear mind in a language-barrier situation: I remember the smell of disinfectant at Ortopedico Rizzoli and the endless corridors there. One fracture, two titanium cables, three steel needles, five exams, forty-degree of heat, and the endless cycles of rehabilitation training. I swallowed the most delicious panino with porchetta from a small stall near Basilica di San Francesco in Assisi, then dived straight into studying, exams, and my thesis.

Life was full of challenges, but giving up is never in my dictionary. The situation makes me remind my life in high school: I was like the bottom student in the best high school in China, but I never gave up my passion for physics and astronomy despite one setback after another. Perhaps, it was the stars in the city's mid-nights and the observations organized with the astronomy club that encouraged me to emerge from those dark times. It was like this six years ago, and it is like this today. The difference is that, six years later, I have gained countless genuine friendships and guidance in another country. I don't feel like I've been fighting a lonely battle, but rather growing into a stronger person with everyone's companionship. Therefore, I would like to express my most sincere gratitude to many, many people.

Thanks to my outstanding supervisors, **Prof. Leonardo Testi** and **Dr. Lorenzo Pino**, who, in my most difficult moments, provided the greatest understanding and assistance. Their wealth of knowledge and keen academic insights guided me into a fascinating academic world: the formation and evolution of planets, which I would like to participate more in the next couple of years. Thanks to my friend **Lorenzo Martinelli**, who appeared in many of my bad-luck moments, giving me support from the first instant. Without him, my situation would have been even much worse

¹. I wish him all the best in enjoying a beautiful Ph.D. life in Australia. Thanks to **Daive Marro, Michael Pasquini, Emiliano Pezzini, Mario Spaziante, and Ricardo Jaimes** for accompanying and helping me during the rehabilitation period and comforting me when I was exhausted from exams. Also, thanks to my Chinese friends **Mengyao Zhou, Yue Yu, Hang Luo, Fengyu Lin**, and whom have accompanied me from high school to now: **Yichang Lu** and **Zhuoxi He**. Some of them are in China, some, like me, are studying in Europe. I wish them all the best.

Of course, thanks to my physiotherapist **Luana Mingardi** and the medical team in Ortopedico Rizzoli. Thanks to Erasmus's program for giving me the opportunity to study exoplanet science at the Geneva Observatory, allowing me to systematically understand the theoretical foundations and cutting-edge studies of exoplanets within four months. Thanks to my supervisors of the course Astrophysical Laboratory II in Geneva, **Yinan Zhao** and **Xavier Dumusque**, and my landlord **Fabrizia Zanettin Barbin**.

Thanks to all of my amazing friends in Bologna, **Ardiana Bushi, Leonardo Kupper Tozzi, Lorenzo Vannini, Luca Guglielmi, Enrico Veralidi, Alfonso Pisapia, Kumar Aryan, Matteo Saponi, Gulia Mattioli, Emmanuel Agati, Nicolò Rotella, Michele Costa, Damiano De Angelis, Mahmoud Abdelhay, Amin Fard...** I cannot list everyone, but everyone is in my mind. It's my pleasure to have you as my friend in this journey, and I am grateful for all care and concern: It is your enthusiastic help that has helped me integrate into this vibrant city and university, allowing me to embark on an amazing new life thousands of kilometers away from where I lived for twenty-two years, and once again feel at home.

Finally, thanks to my father, mother, and my family. Thank you for your support every day, and for having complete faith in my ability to live independently. In a city of ten million people, we three, a small but strong-enough family, always support each other and endure countless storms together. Mom, Dad, no matter where I am, you are the people I care most about on this planet. I love you.

¹OR maybe he's my bad-luck himself, causing my misfortune in the first place?...